

REPORT DOCUMENTATION PAGE

AFRL-SR-BL-TR-01-

Public reporting burden for this collection of information is estimated to average 1 hour per response, including gathering and maintaining the data needed, and completing and reviewing the collection of information. Send collection of information, including suggestions for reducing this burden, to Washington Headquarters Services, Davis Highway, Suite 1204, Arlington, VA 22202-4302, and to the Office of Management and Budget, Paperwork Reduction Act, Washington, DC 20585.

0283

1. AGENCY USE ONLY (Leave blank)			2. REPORT DATE	3. REPORT TYPE AND DATES COVERED
			Final 01 Jun 97 to 31 May 00	
4. TITLE AND SUBTITLE (New World Vistas) Three-Dimensional Analysis of the GMBK (Gigawatt Multiple Beam Klystron)			5. FUNDING NUMBERS 2301/EV 61102F	
6. AUTHOR(S) Dr Smithe				
7. PERFORMING ORGANIZATION NAME(S) AND ADDRESS(ES) Mission Research Corp P.O. Drawer 719 735 State Street Santa Barbara, CA 93102-0719			8. PERFORMING ORGANIZATION REPORT NUMBER	
9. SPONSORING/MONITORING AGENCY NAME(S) AND ADDRESS(ES) Air Force Office of Scientific Research 801 N. Randolph Street Arlington, VA 22203-1977			10. SPONSORING/MONITORING AGENCY REPORT NUMBER F49620-97-C-0019	
11. SUPPLEMENTARY NOTES AIR FORCE OFFICE OF SCIENTIFIC RESEARCH (AFOSR) NOTICE OF TRANSMITTAL DTIC THIS TECHNICAL REPORT HAS BEEN REVIEWED AND IS APPROVED FOR PUBLIC RELEASE LAW AFR 190-12. DISTRIBUTION IS UNLIMITED.				
12a. DISTRIBUTION AVAILABILITY STATEMENT Unlimited Distribution				
13. ABSTRACT (Maximum 200 words) The basis of this work is the 3-D simulation analysis and assessment of the GMBK design performed with the Stanford Linear Accelerator Center (SLAC). A 19-beam hexagonal-packed Multiple Beam Klystron was of interest to SLAC. The emphasis of the project, especially in the final 12 months became the assistance and collaboration with SLAC on issues relating to simulation design, primarily with 3-D simulation tools, but also with existing 2-D simulation tools. This has included a comparison of predicted results with experimental data, often on fairly contentious issues, where simulation and past experience have not pointed in the same directions.				
14. SUBJECT TERMS				15. NUMBER OF PAGES
				16. PRICE CODE
17. SECURITY CLASSIFICATION OF REPORT Unclassified	18. SECURITY CLASSIFICATION OF THIS PAGE Unclassified	19. SECURITY CLASSIFICATION OF ABSTRACT Unclassified	20. LIMITATION OF ABSTRACT UL	

**THREE-DIMENSIONAL ANALYSIS
OF THE GMBK
(GIGAWATT MULTIPLE BEAM KLYSTRON)**

Final Report

MRC Contract: 97051.01
AFOSR Contract: F49620-97-0019

David N. Smithe

January 22, 2001

Prepared for:

Air Force Office of Scientific Research
801 North Randolph Street, Room 732
Arlington VA 22203-1977

Prepared by:

Mission Research Corporation
8560 Cinderbed Rd., Suite 700
Newington, VA 22122
703-339-6500

20010427 100

Table of Contents

TABLE OF CONTENTS.....	2
1. EXECUTIVE SUMMARY.....	3
2. ORIGINAL GMBK.....	4
2.1 GMBK GEOMETRY.....	4
2.2 TOROIDAL CAVITY MODE STRUCTURE	4
3. 19-BEAM MBK.....	7
3.1. MULTIPLE BEAM GEOMETRY	7
3.2. MULTIPLE BEAM PROPAGATION.....	10
3.4. MULTIPLE BEAM OUTPUT CAVITY.....	14
3.5. MULTIPLE BEAM SUMMARY	15
4. ADVANCES IN 3-D SIMULATION METHODS.....	16
4.1 BEAM LOADING	16
4.2. INTERACTIVE 3-D GEOMETRY VIEWER.....	18
4.3. FULL SPECTRUM CHARACTERIZATION	21
4.4. VOLTAGE AND CURRENT PHASE	23
4.5. EVOLUTION OF THE RF CURRENT	24
5. NEW SIMULATION MODELS.....	28
5.1 SURFACE RESISTIVITY ALONG A METALLIC WALL.....	28
5.2. THE RESONANT PORT MODEL.....	32
6. A FUTURE MODEL, SMOOTH BOUNDARY MODELING	43
6.1 EXTRINSIC-FINITE-DIFFERENCE.....	44
6.2 POYNTING'S THEOREM AND POYNTING FLUX.....	45
6.3 DISCONTINUITY OPERATORS.....	47
6.4 ROADMAP.....	47
7. HIGH PERVEANCE KLYSTRON ISSUES.....	57
7.1 THE HIGH FREQUENCY SCALING PROBLEM	57
7.2. THE HIGH PERVEANCE KLYSTRON GALLERY.....	58
7.3. FREQUENCY SCALING FOR HIGH PERVEANCE SOLUTIONS	61
7.4. DESIGN PARAMETERS TO DATE.....	62
7.5. CAVITY ISSUES.....	65
REFERENCES.....	72

1. Executive Summary

The basis of this work is the 3-D simulation analysis and assessment of the GMBK design, to be performed in close contact with personnel at the Stanford Linear Accelerator Center (SLAC). A secondary aspect of the project is assist in the design of such GMBK features as may be desired by SLAC. And finally, a tertiary aspect of the project is to compare predicted results with actual experimental data. However, within weeks of the start of this project, the GMBK project became of secondary concern to SLAC, and it became clear that there would be no experimental data from such a device, as it was unlikely to be constructed within the term of this project. Indeed no further design work at SLAC was anticipated either. Instead a 19-beam hexagonal-packed Multiple Beam Klystron was of interest to SLAC. Thus some of the focus shifted from the GMBK to the 19-beam MBK device. However, there was also direction from the sponsor to not become overly focused on one particular design or device.

This being the case, the emphasis of the project, especially in the final 12 months, became the assistance and collaboration with SLAC on issues relating to simulation design, primarily with 3-D simulation tools, but also with existing 2-D simulation tools. This has included a comparison of predicted results with experimental data, often on fairly contentious issues, where simulation and past experience have not pointed in the same directions. The result of this entire collaboration, has, however, been very beneficial in three ways: 1) Simulation tools have been brought into a state which more adequately address the needs of the klystron designers at SLAC, 2) Designers at SLAC have had access to design tools of a type and quality not previously available to them, which has led to improved understanding (and even reversed understanding, in at least one case) of issues of importance to higher frequency regimes, where experimental data and experience is still nascent, and 3) programmers at Mission Research Corporation have been made more aware of design issues, and the need for simulation tools to provide design information directly and efficiently.

The final test of success, though, is that SLAC personnel continue to routinely utilize the tools and methods developed throughout this project for the design of new klystrons in new regimes. And if the numerous SLAC-MRC phone and e-mail inquiries of the past several months (post GMBK-contract !) are any indication, it is likely that the breadth of application for these tools and methods is capable of growing still more, if allowed to. For myself (DNS), I would like to state that this collaboration with SLAC has been the most scientifically challenging and rewarding effort in which I've been engaged in for many years, and I am very appreciative of the opportunity to broaden my perspective and understanding of klystron design issues, and to bring this new understanding to bear on the quality of the 3-D simulation tools which MRC prides itself on.

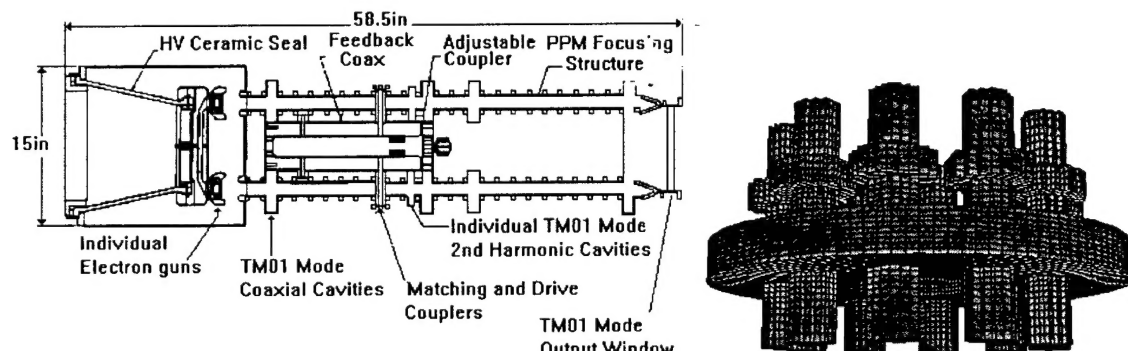
2. Original GMBK

This material relates to the original GMBK design. While most of this work was done as preparation for the proposal, it is included here for completeness, and also in the event that interest in the original GMBK design should reappear some time in the future, there may be need to refer back to it.

2.1 GMBK Geometry

The goal of the Multiple Beam Klystron (MBK) is to meet the challenge of producing one or more gigawatts power at a frequency of 1 GHz for directed energy applications. A baseline concept, the GMBK (Gigawatt Multiple Beam Klystron), has been forwarded by George Caryotakis¹ and coworkers at SLAC. The GMBK is a result of the Air Force's MURI program and its focus on gigawatt, kilojoule sources for directed energy applications. The MBK was reinvented in the "Western Consortium" of MURI (Stanford and UC-Davis). The technical requirements of GMBK include high efficiency and high vacuum for power handling. The innovation of the baseline concept is the use of Periodic Permanent Magnets (PPM's) to remove the solenoidal field, thus providing higher efficiency. The relatively low perveance of the individual beams makes them relatively easy to focus with a PPM

The GMBK, shown schematically in figure below, with a 3-D illustration of a simulated cavity, contains some unique three-dimensional features, whose behavior has yet to be experimentally established. This includes the multiple beam-line PPM system, the coaxial buncher cavities, the coaxial feedback system, and the output cavity-coupler-collector geometry. The initial year of the computational analysis will focus on these aspects of the device.



GMBK design and 3-D simulation geometry of 2nd harmonic cavities and coaxial buncher cavity.

2.2 Toroidal Cavity Mode Structure

The toroidal input and buncher cavities are designed to operate in the TM010 mode, which is the lowest frequency mode supported by the cavities. This is a very favorable condition for successful operation. However, the cavity is also long in one direction, the azimuthal, compared to the other two directions, e.g., radial and axial. This

leads to “bands” of closely spaced azimuthal modes at each of the radial and axial modes, including the fundamental. The closeness of the azimuthal modes to the operating frequency is a potential area of concern.

An eigenmode scan of the geometry shown in the figure was performed to calculate the lowest eight modes of the GMBK cavity (mode nomenclature corresponds to coaxial transmission line modes):

<u>f (GHz)</u>	<u>Mode ($N_\phi N_r N_z$)</u>
1.546	TM010
1.613	TM110
1.765	TM210
2.040	TM310
2.334	TM410
2.600	TM510
2.722	TM610
3.002	TM020

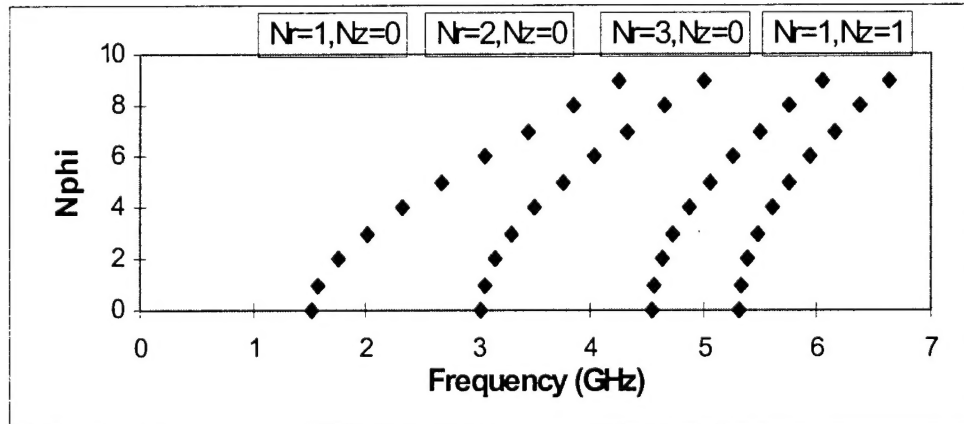
As one might imagine, the modes fit quite closely to the following formula, derived from “unwrapping” the toroidal cavity into its equivalent rectangular volume:

$$f_{N_\phi N_r N_z} = c \sqrt{\left(\frac{N_\phi}{\pi(R_{in} + R_{out})}\right)^2 + \left(\frac{N_r}{2(R_{out} - R_{in})}\right)^2 + \left(\frac{N_z}{2L_z}\right)^2}$$

$$= c \sqrt{2.174 N_\phi^2 + 25.48 N_r^2 + 288.0 N_z^2}$$

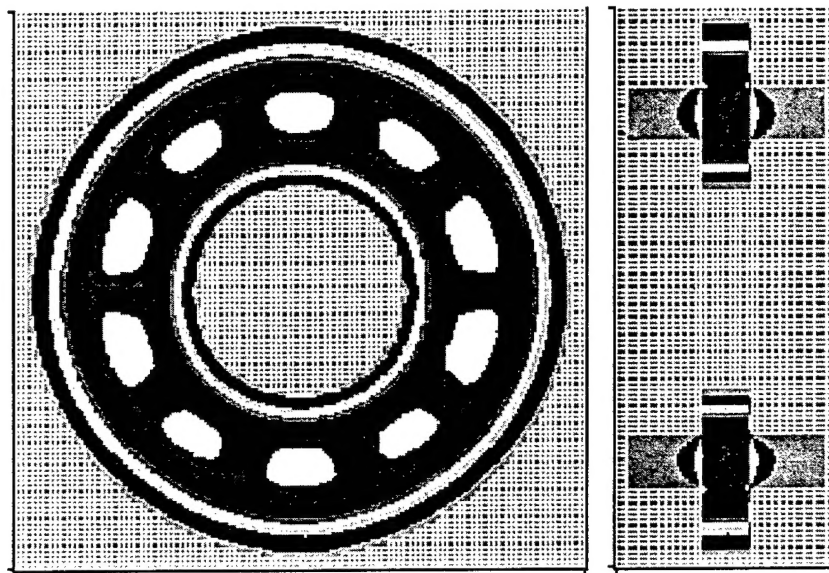
These modes are illustrated in figure below..

The figure illustrates the band of modes near the fundamental. In particular, note that the TM110 mode is only 66 MHz (4%) from the operating frequency and, that at least seven modes occur before the second harmonic of the operating frequency. There are no TE modes below 5 GHz because of the short axial cavity dimension. The TM010 operating mode is illustrated in following figure.



Banded mode structure of coaxial buncher cavity. Note proximity of low frequency modes.

The $N_{\phi} \neq 0$ modes are of particular concern. These modes can couple strongly to the beams and can be driven by differences between the beam-lines in current, voltage, or incoming bunch amplitudes. The signal input into the first cavity is expected to be delivered symmetrically and should not excite $N_{\phi} \neq 0$ modes.



Simulation of operating mode in coaxial buncher cavity, complete with drift tube sections.

3. 19-Beam MBK

The MAGIC3D simulation code was used to assess the multi-dimensional physics issues relating to the design and operation of a multiple beam klystron. Investigations include a detailed study of the mode structure of the cavities in the 19-beam hexagonally packed geometry and a study of the velocity spread caused by the cavity mode's field profile. Some attempts to minimize this effect are investigated. Additional simulations have provided quantification of the beam loading Q in a dual input cavity, and optimization of a dual output cavity.

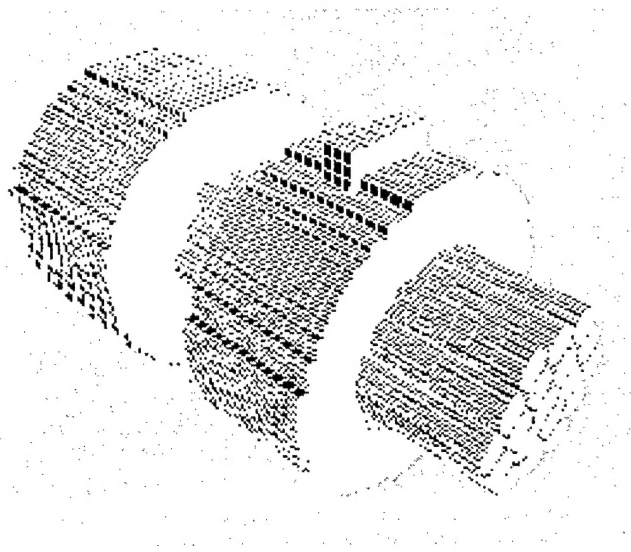
An important goal of the simulations is an accurate picture of beam transport along the length of the MBK. We have quantified the magnitude and spatial variation of the beam-line space charge interactions within a cavity gap. Present simulations have demonstrated the transport of the beam through three cavities (the present limits of our simulation size) without difficulty; additional length simulations are expected. We have also examined unbalanced beam-line scenarios, e.g., one beam-line suppressed, and find little disturbance to the transport in individual cavity tests, with results for multiple cavity transport expected.

3.1. Multiple Beam Geometry

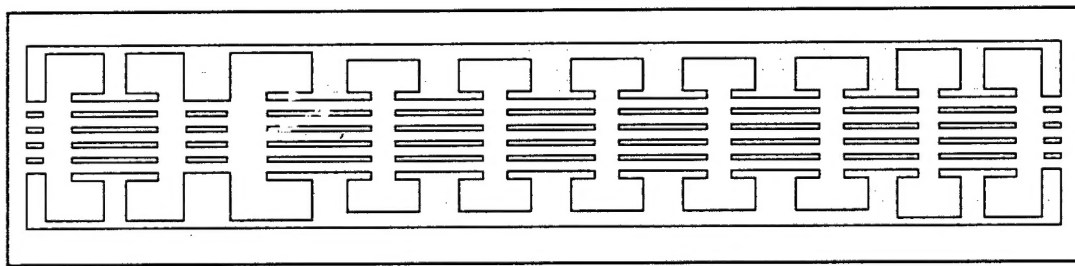
Multiple beams are a well established means of increasing beam permeance, e.g., the total beam current relative to the beam space charge potential. Multiple beam klystron (MBK) technology is well established in Russia.ⁱⁱ In the US, the MBK is under consideration at higher voltage and power levels.ⁱⁱⁱ Each beamline of an MBK travels in its own drift tube, and has a nominal single beam permeance. However, all beamlines enter into the same cavity structure, and within the cavity the total beam permeance can be significantly greater than 2 micropervs. The great advantage of the multiple beam approach is that each drift tube is still cut-off at the operating frequency, just as with a conventional klystron. Hence there is minimal danger of direct RF-communication between stages of the klystron which could lead to oscillation. Other means of increasing beam permeance, such as planar or cylindrical sheet beams must invariably use drift tubes which are not cut-off, and hence these latter devices require very careful tuning and/or damping of the cavity and drift tube structure to prevent communication between cavities.

This paper is primarily devoted to the hexagonally packed arrangements of multiple beams. An alternative annular arrangement of beams, is presented in Reference 2 and may also prove interesting, because of its potential to use permanent magnet focusing. A significant feature of the hexagonally-packed MBK cavity is its good mode separation between the lowest mode, which is the operating mode, and the next highest mode of the cavity. In this manner, the hexagonally packed MBK still resembles the typical klystron. Other high permeance beam geometry's, (including annular arrangements of multiple beams) usually require cavity structures which have poorer mode separation near the operating mode.

The figure below shows the simulation grid used for representing a 19 beam hexagonally packed multiple beam klystron (MBK). As with many three dimensional simulations grid resolution is the primary challenge. Each individual drift tube fits within a 9x9 cell cross section, and the electron beam itself is about 5 cells across. Length is also a challenge, and typically three cavities are possible in a single simulation, to date. The figure shows the diode region and an input cavity. The 19 beamlines penetrate the input cavity. A small waveguide aperture is used to couple energy into the input cavity.



View of three-dimensional simulation grid for a 19 beam hexagonally packed multiple beam klystron (MBK). The diode region and an input cavity are shown, with 19 individual beamlines penetrating each.



Schematic of 10 cavity MBK klystron of interest to SLAC.

The primary restriction on hexagonally packed MBK's is that the total cross-section of the multiple beam arrangement not exceed half a free-space wavelength, in order to insure that the cavity remains in a well separated fundamental mode. For reasonable single beam size and drift tube wall thickness, this restricts the number of beams, and hence the hexagonally-packed MBK's have an intrinsic limit on the perveance. No such limit exists on other high perveance beams, such as the annular arrangement of multiple beams or planar and cylindrical sheet beams, since in principle, at least, they can be widened ad infinitum. Conceptually, then the hexagonally packed MBK may be thought of as an "intermediate" method of enhancing beam perveance. It retains the drift tube

and cavity properties of traditional klystrons, but multiplies the current limit by the number of beams, which can typically be 7, 19, 37, or perhaps even 61. Alternate methods have, in principle, no current limit, but must suffer the obvious difficulties associated with having a beam dimension greater than half a free-space wavelength.

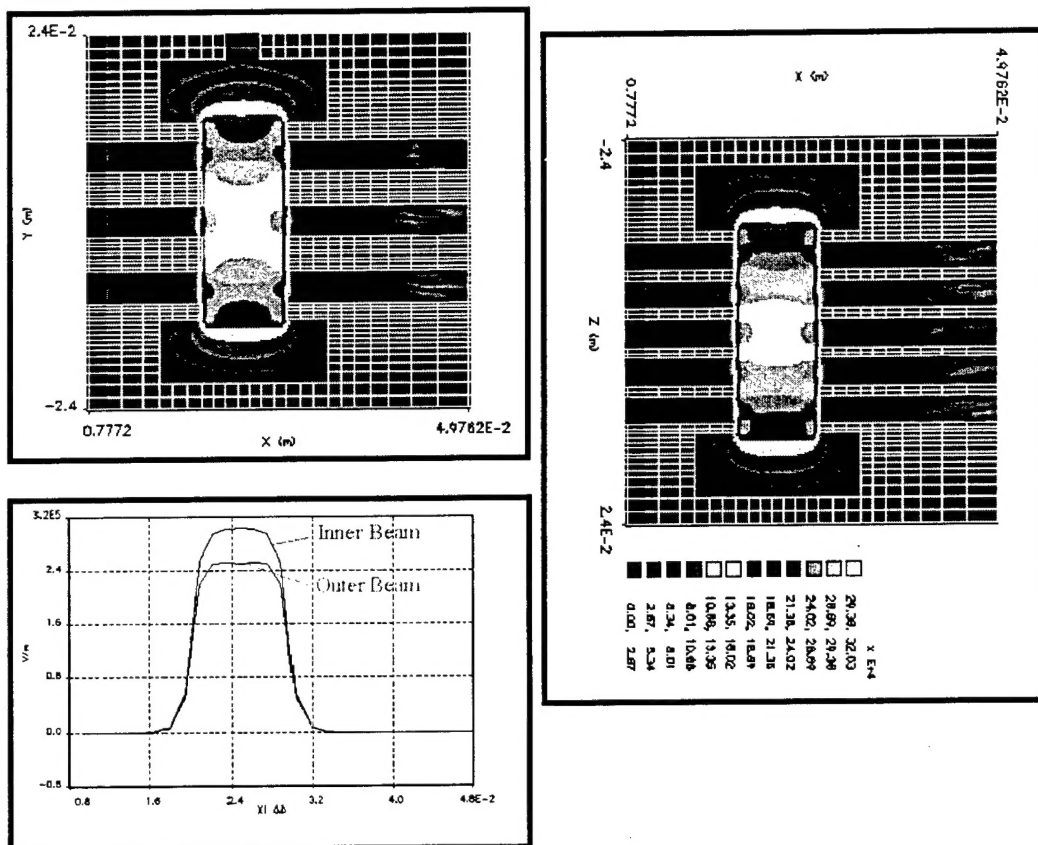


Illustration of the MBK cavity mode structure. Both the 3-beamline and 5-beamline planes are shown. The electric field profiles in the inner and outer beam lines are compared.

The hexagonally packed MBK's have a disadvantage not shared with other high permeance beam arrangements. This disadvantage is an inherent nonuniformity in the interaction field strength across the beams. Except for the hexagonally packed MBK, all high permeance schemes have operating modes which possess a uniform field across the entire beam. The fairly traditional cavity structure of the hexagonally-packed MBK implies that the center beamline experiences a larger net voltage across the gap than the outer beamline. This is a consequence of Stokes Theorem, which indicates that if the profile were flat, then no magnetic field, and hence no Poynting flow could exist in the region. The result is a spread of the velocity modulation from one beam line to another, which can slightly decrease the ideal efficiency of the device, at least in comparison to the number of beams multiplier. Note that an annular arrangement of multiple beams does not possess this property. (In most manners concerning the cavities, an annular

arrangement of multiple beams more closely resembles a sheet beam, rather than a hexagonally-packed MBK.)

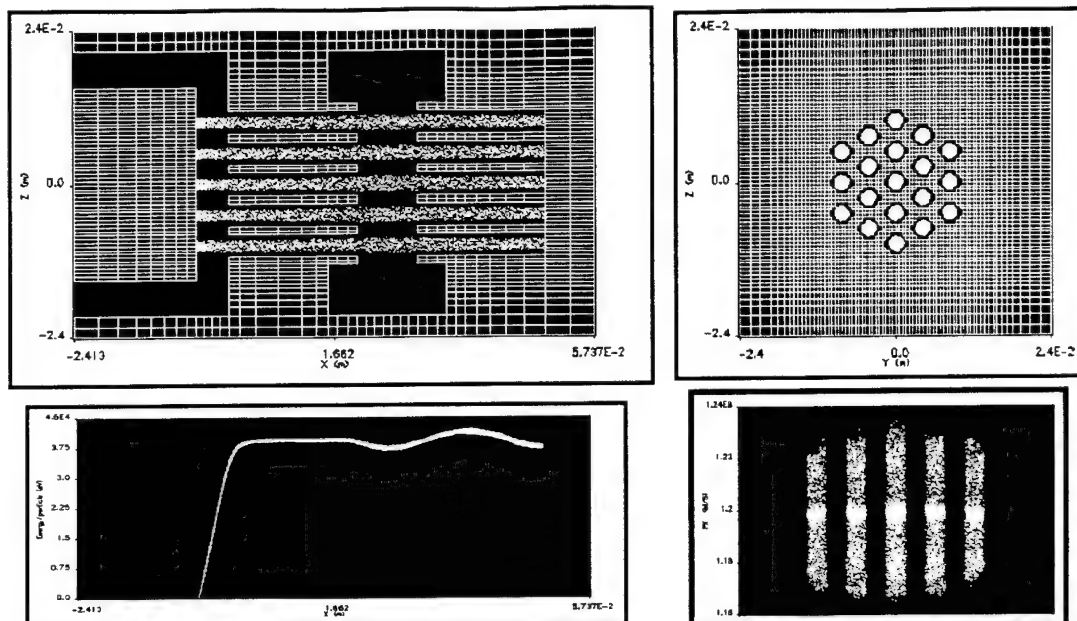
The following figure shows the operating mode of a 19-beam MBK. The two cut-planes through the center cut through either three or five beamlines. The innermost beam sees a 14% stronger RF field in the cavity than does the outermost beam. Shaping of the inner cavity walls may not affect RF voltage directly, but it can affect the transit angle of the beam, which could have the same desired result of more uniform modulation. Hence, careful tailoring of the inner walls can be used to offset this effect.

3.2. Multiple Beam Propagation

The following figure shows a simulation of a 19 beam MBK, including diode and input cavity. The diode geometry is highly simplified, and uses a magnetic lens in each beamline to provide focusing. The purpose of including the diode is simply to achieve a realistic velocity spread from the acceleration. A 40 kV diode voltage is imposed, and a total of 50 amps current is produced, corresponding to a sum total permeance of 6.25. The individual beamline permeance is 0.33. An energy spread of 560 kV from the diode is observed, which is consistent with the individual beam current of $50/19=2.63$ amps.

The input cavity in the previous figure receives power and modulates the beam. The gap voltage is about 6 kV. A detailed investigation of the beam loading indicates a value near about $Q=80$. This value is found by loading the cavity with power prior to injecting the beam, and then observing the decay rate of the cavity oscillation once the beam is turned on. The large beam loading is typical of MBK's and may permit them to operate with wider bandwidth than single beam klystrons.

A principle area of interest for MBK's is the transport of the multiple beams through several cavity gaps, since the individual beams do see one another in the cavity gap region. A simple illustration of the level of this effect is to examine the DC electric potential within the cavity when the multiple beams are present. The following figure shows the potential, which drops 0.8 kV from wall to the center of the cavity. The expected potential drop across a single beam of 50 amps is 3.75 kV ($=\mu_0 I_{beam} c / 4\pi\beta$), hence the multiple beam experiences only 1/5th the space charge depression in the cavity that a single beam of the same total current would. This reduction is due to the close proximity of the cavity and drift tube walls, which are interspersed within the multiple beam stack.



A 19 beam hexagonally-packed multiple beam klystron simulation. Shows the diode, input cavity, energy evolution, and axial momentum in the various beam lines. The energy rises from zero at the cathode to 40 keV, and then is modulated in the input cavity. The energy spread from the anode in the 50 amp (6.25 μ peravs) beam is 1.4%, and the RF modulation is about 14%.

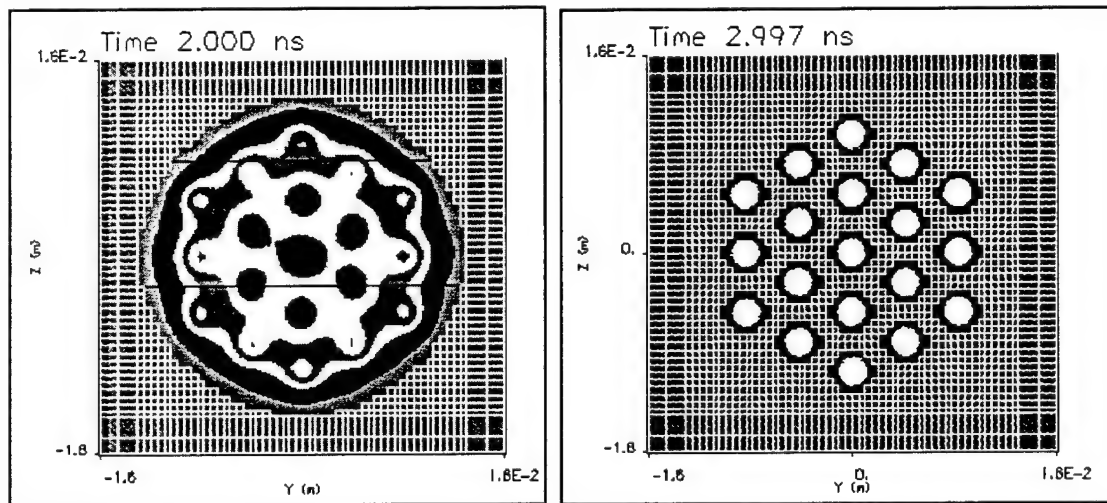
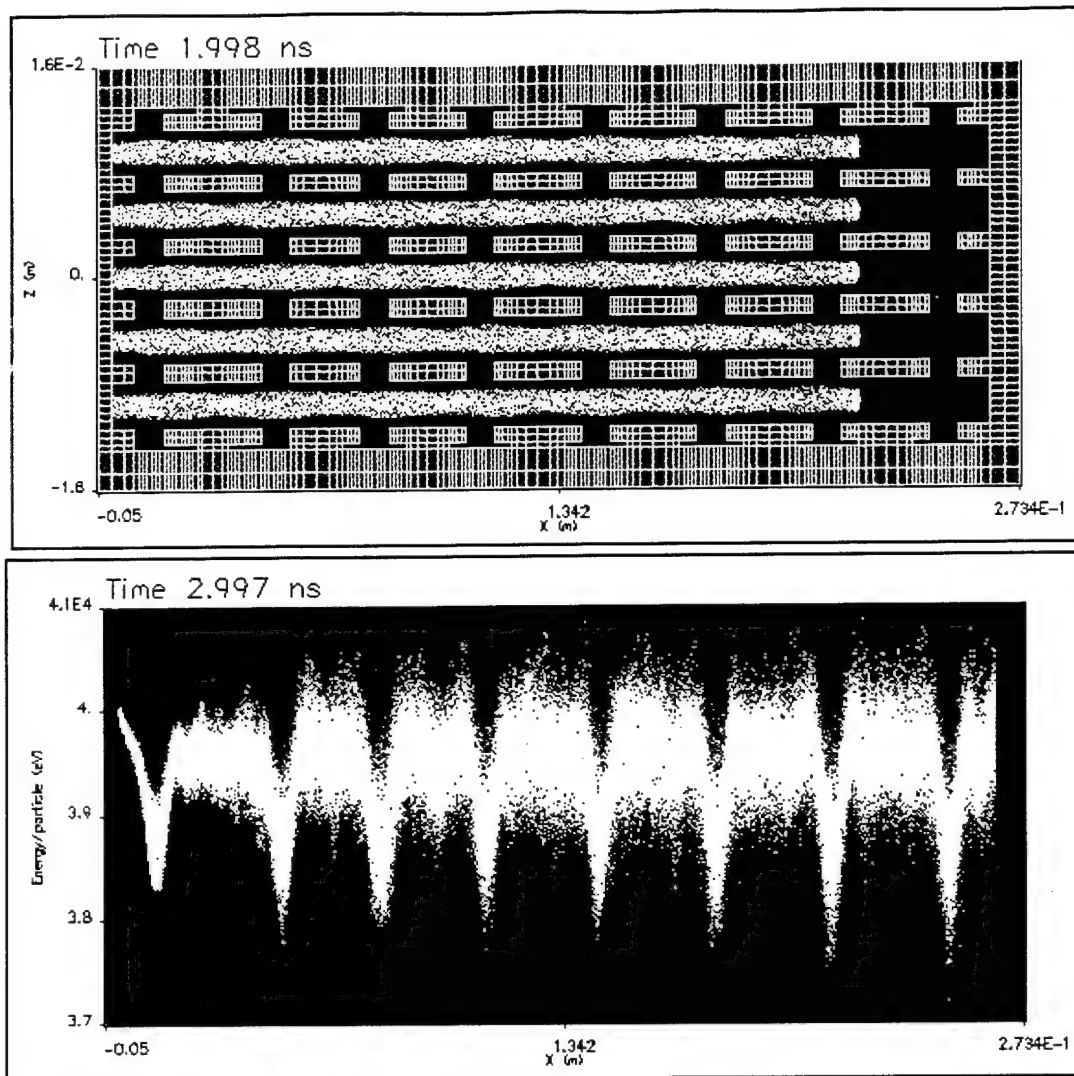


Illustration of electrostatic potential within the cavity. The potential drops 0.8 kV at the center. This is 1/5th the space charge depression which would occur for a single beam of the same total current. Hence, even in the cavity, the beam-beam interaction is greatly reduced.

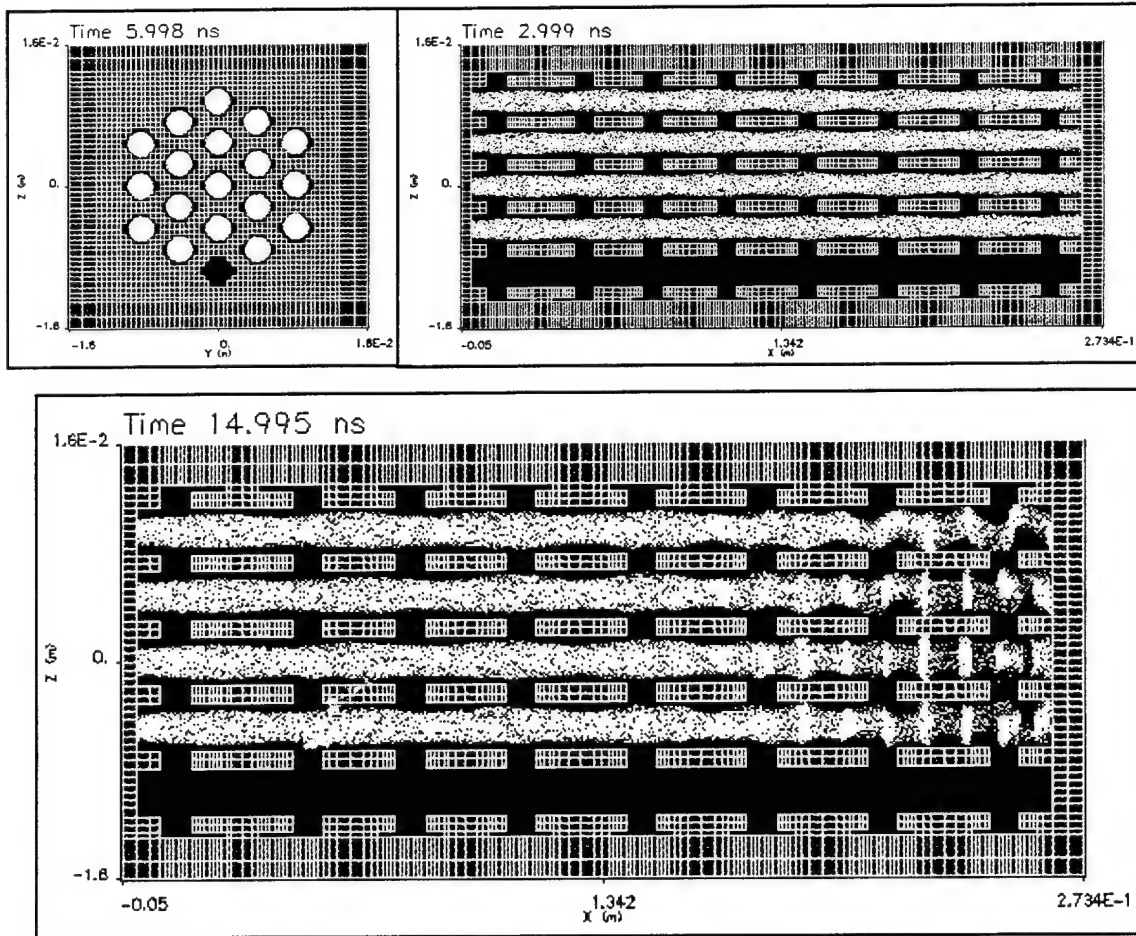


Transport of unmodulated multiple beams through 8 cavity gaps. There is a 1 keV visible drop in cavity gaps, together with a 1 keV energy spread, after the first two cavities. The beam is confined without losses by a perfect solenoid field, at 1.3 x Brillouin. The outer part of the cavities are removed to save finite-difference cells.

The figure above shows a simulation with eight gaps. This simulation was constructed in order to observe the behavior of the beams through several cavities. In this run, the beam is emitted at full energy on the left, and travels through eight gaps before striking the wall on the right. A uniform magnetic field at 1.3 times the Brillouin field was used to confine the beam. To perform this simulation it was necessary to remove the outer part of the cavities, in order to have a reasonable number of cells. Hence any RF in this particular geometry is highly unrealistic; what is of interest is simply the DC behavior. It is observed that after propagating through only two gaps, the beam has a 1 keV spread, which persists without growing through the remaining six gaps. The 1 keV spread is consistent with the previously noted potential drop of 0.8 kV. In addition, at each gap,

the beam energy dips the expected 0.8-1.0 keV. The simulation was run out to 50 nanoseconds without any apparent change in the DC state.

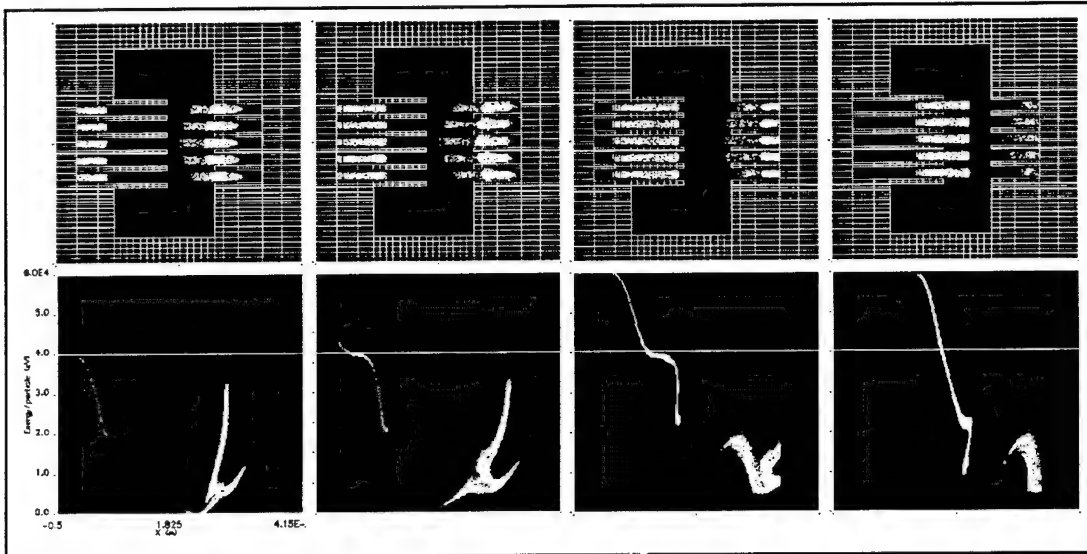
The successful transport of an unmodulated beam through eight gaps seems well demonstrated by the simulation in the figure below. Future work will investigate the transport of a density and velocity modulated beam. Based partly on the output cavity simulations below, it is likely that the major difficulties will be single beamline issues, though, e.g., radial expansion of the individual beams in the output region, rather than beam-beam effects accrued in cavity gap passes.



Highly distorted geometry illustrating a beam-beam oscillation. One beamline is removed to create a severe asymmetry, and the highly distorted cavity geometry can easily oscillate at frequencies which are not cut-off in the drift tubes. No such oscillation is observed in realistic cavity geometry, or when the beam line asymmetry is weaker in the distorted geometry. This test case illustrates the capability of the simulations to detect and model such modes if and when they are present.

An extreme situation which might present some possibility for beam-beam interactions to occur is a large scale asymmetry in the beamlines. In an attempt to determine some kind of threshold for undesirable beam-beam interaction (!), the simulation of this figure was altered, so that one of the outer beamlines was turned off.

The results of this alteration are shown in figure below. After about 15 nanoseconds a dramatic oscillation is apparent. This oscillation is clearly not an axisymmetric mode. In addition it has a very high frequency because of the shortened cavity radius. The oscillation frequency is sufficiently high that propagation in the individual beam tubes is possible, and it was observed that the oscillation rapidly propagated to the left, towards the beam emission site. The cavity geometry for this test case is so distorted that this result must not be interpreted as a physical demonstration of actual MBK behavior. It must be considered to be merely a demonstration of the capabilities of the simulation technique, e.g., 3-D non-axisymmetric oscillation modes, if they are present, can indeed be modeled in these simulations. Nevertheless, given that removal of a beamline was the trigger which initiated the behavior seen in the figure, it is clear that achieving good symmetry among the beamlines is important, especially for preventing growth of non-axisymmetric modes.



One cycle of an idealized output cavity simulation. Beam is created with favorable density and velocity pre-modulation and the low density portion of beam is omitted to improve visualization. Very high efficiency was obtained. The challenge for future simulations is to complete an end-to-end MBK simulation resulting in similar favorable performance.

3.4. Multiple Beam Output Cavity

Simulations of an output cavity for the 19 beam hexagonal-packed MBK were performed. The cavity is illustrated in next figure. The beam is created with RF current density of about $I_1/I_0=1.75$, and velocity modulation equal to half the average beam energy, with a temporal profile which is favorable for high efficiency power extraction. The low density part of the beam is removed from the figure to improve visualization. All beamlines are emitted in synchronous phase. Based on the average particle energy reduction, an efficiency of greater than 50% is obtained. (An exact figure is not available for this run.) The same cavity voltage profile effect which occurred in the input cavity

affects the output cavity, as can be seen by the greater slowing of the center beamline compared to the outer beamlines. This strong beamline shear in the output cavities probably prevents multiple output cavity structures from having more than two or maybe three cavities.

To test the integrity of the output circuit vis-à-vis beam asymmetries, the same run was repeated with one beamline missing. No occurrence of unusual behavior was detected, and the velocity modulation amplitude reduced by the expected factor of 18/19. The beam propagation appears quite robust. Both output cavity runs show the beam scraping on the individual beam tube walls after the output cavity gap. This indicates a need to increase the magnetic field above 1.3 Brillouin, or reduce beam fill factor, or shape pole pieces better. Indeed the MBK collector presents a difficult choice. Simplest is to have a single collector for all of the beamlines. However, such a large volume would have to be carefully tuned, to prevent spurious oscillations within its volume. Alternately, individual collectors for each beam line could be used, but this presents difficulties because of the natural expansion of the beam after passing through the output cavity, and the difficulty in heat removal from the long thin drift tube walls.

3.5. Multiple Beam Summary

The MAGIC3D simulation code was used to assess multi-dimensional physics issues relating to the design and operation of multiple beam klystrons. Investigations of MBK geometry, beam propagation and output structures have been performed. To date, all indications are that high power implementations of the multiple beam klystron concept are indeed feasible. In particular, the beam transport issue is likely to be important only at the output end of the device, and even this difficulty is not related to beam-beam interaction.

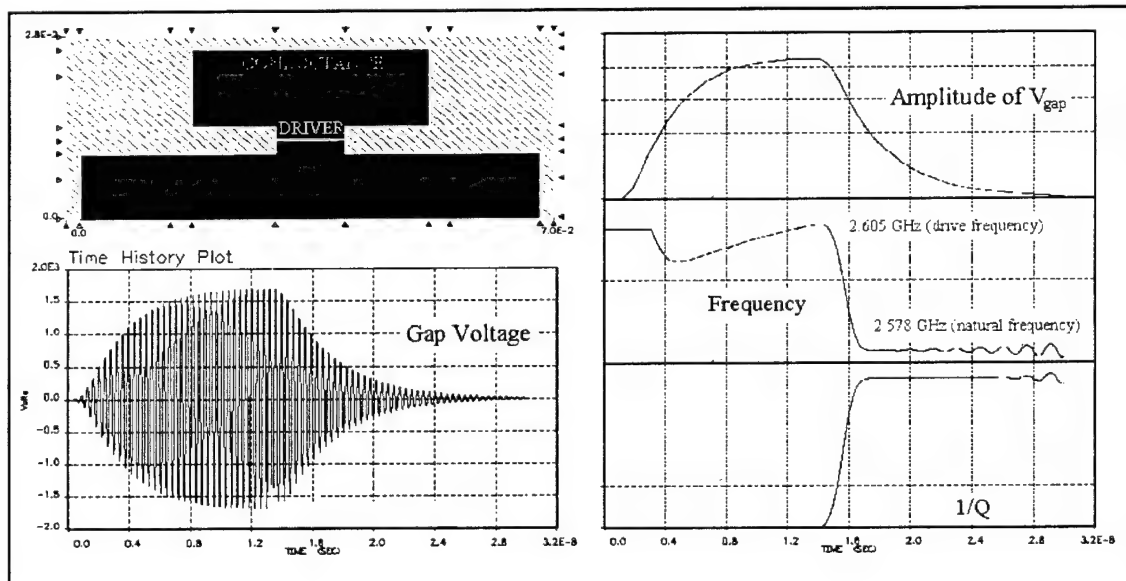
An important goal of the simulations is an accurate picture of beam transport along the length of the MBK. The challenge for the future is to tie together the various pieces of the MBK picture, for a more complete end-to-end analysis, within the constraints of a feasible calculation. Steps to devise more effective methods of simulating the physics, and to better approximate aspects of the structure are being implemented, including a resonant port model, which should remove much of the need for the large cavity volumes, and greatly reduce the simulation size.

4. Advances in 3-D Simulation Methods

In any simulation project, often it is not so much the fundamental algorithms of the simulation tool which provide the desired information, it is the clever way in which the tool is used to generate the information that matters. And often, the successful simulation depends on some non-trivial operations performed with the raw data, e.g., on a sophisticated diagnostic. The past three years have seen dramatic improvement in the methods in which the simulation tools are used to generate useful engineering information. Much of this improvement follows a simple approach – duplicate the same measurement done in the laboratory. This section details some of the new and improved methods which have been developed during this project.

4.1 Beam Loading

Early on in this project, Dr. Daryl Sprehn from SLAC spent a week at the MRC offices to acquaint himself with the MAGIC simulation tool, and to perform a very specific task with the tool. The task was to determine the beam loading of a cavity. In cold-test, e.g. before the beam is present, the cavity has a resonant frequency and a loss parameter, Q, indicating power losses to the walls, or couplers if there are any. Once the beam is added, the frequency and Q change slightly because of the presence of the beam, which is, after all, a plasma now within the system, which both changes the effective permittivity and acts as an additional power sink.



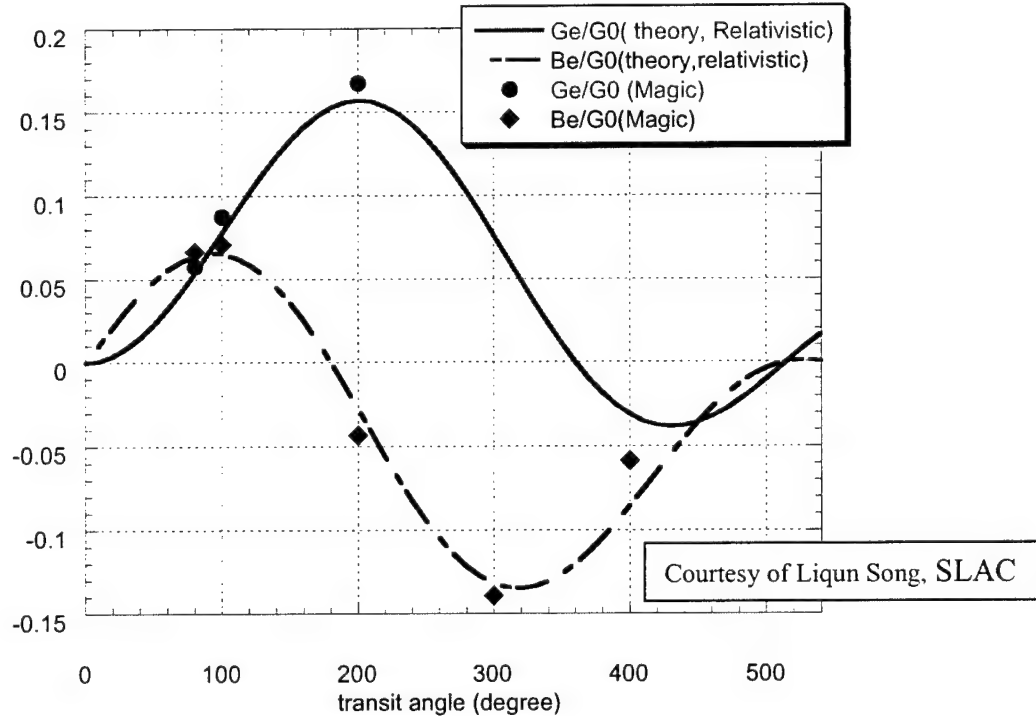
A ring-up / ring-down simulation to determine loaded frequency and Q of a cavity.

After much thought, it was decided that the obvious way to determine the change in frequency and Q was to perform a “ring-up/ring-down” simulation. This proceeds as follows, the beam is injected through the drift space before the cavity has been excited. Then the cavity is excited at the cold test frequency for, say 20 cycles, then the excitation is turned off, and the cavity rings and decays. A special diagnostic was created to very

accurately determine the instantaneous frequency, and to measure the Q from the decay rate. Output from such a simulation is shown above. The drive frequency is 2.605 GHz, but when the drive turns off, the cavity relaxes to a frequency of 2.578 GHz.

Unfortunately, when the actual beam and cavity of interest to SLAC were simulated in this manner, the frequency was seen to shift upward, which is counter to all previous experience and intuition ! The issue remain unresolved for over a year, as all attempts to find fault with the simulation methods failed, and all attempts to explain the results in physical terms also failed. A true controversy, as one might say.

Finally, Dr. Caryotakis of SLAC discovered a textbook (written in French !) that had analytic solutions of precisely the beam loading, in the case of highly simplified geometry, e.g., a pillbox cavity with no drift tube. The analytic formulas indicated that the beam loading could cause either an upshift or a downshift depending on the transit-angle (transit time) of the beam across the cavity. This was one hint that the simulations might be correct. Ultimately, simulations (by SLAC's Liqun Song) were performed of the simplified geometry to match the textbook. The results, illustrated below indicate that MAGIC simulations are indeed an accurate predictor of beam loading. The blue line is a measure of (minus) frequency shift. It can be seen that when the transit angle exceeds 180° the sign of the frequency shift changes.



Comparison of analytic and simulation predictions of frequency and power loading on an ideal cavity. The excellent agreement helped resolve a disagreement between simulation predictions and expected behavior.

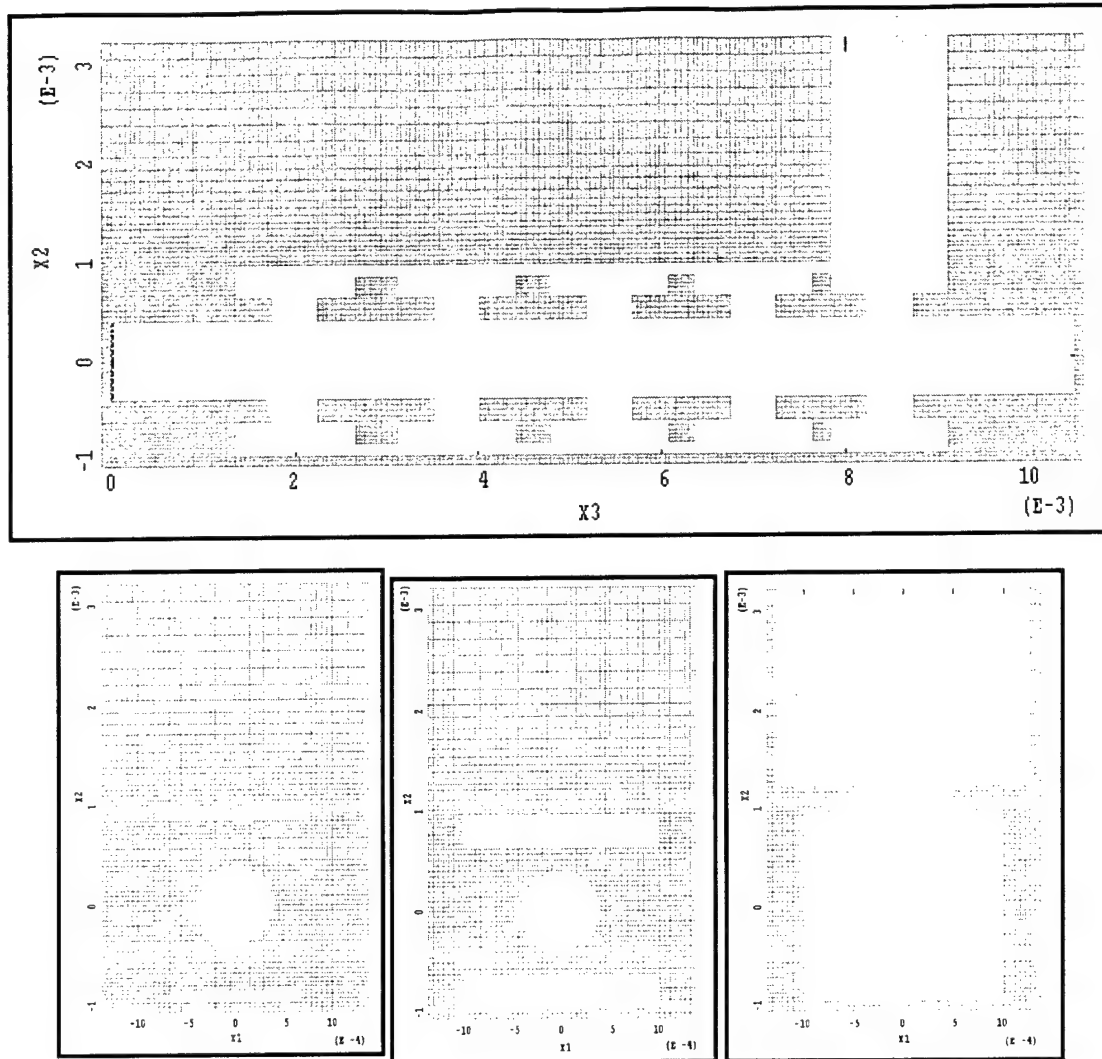
What happened with the original assumption about a downward shift in frequency? Simple, this cavity was at a higher frequency, and had a larger drift tube in relation to the cavity radius than most previous experience. Larger drift tubes tend to result in wider field profiles in the drift tube, which in turn results in wider transit angles, which can result in frequency upshift. This has implications for MBK's, and sheet beam klystrons. The MBK's tend to have small drift tubes compared to the cavity, and thus follow traditional experience of a frequency downshift. The Sheet Beam klystrons tend to have large drift tubes, and have also been seen to experience frequency upshift, instead of downshift.

Bottom line – a new method, including a new diagnostic, was devised to examine a classic design question. The results, although initially controversial, have resulted in improved understanding of the classic question.

4.2. Interactive 3-D Geometry Viewer

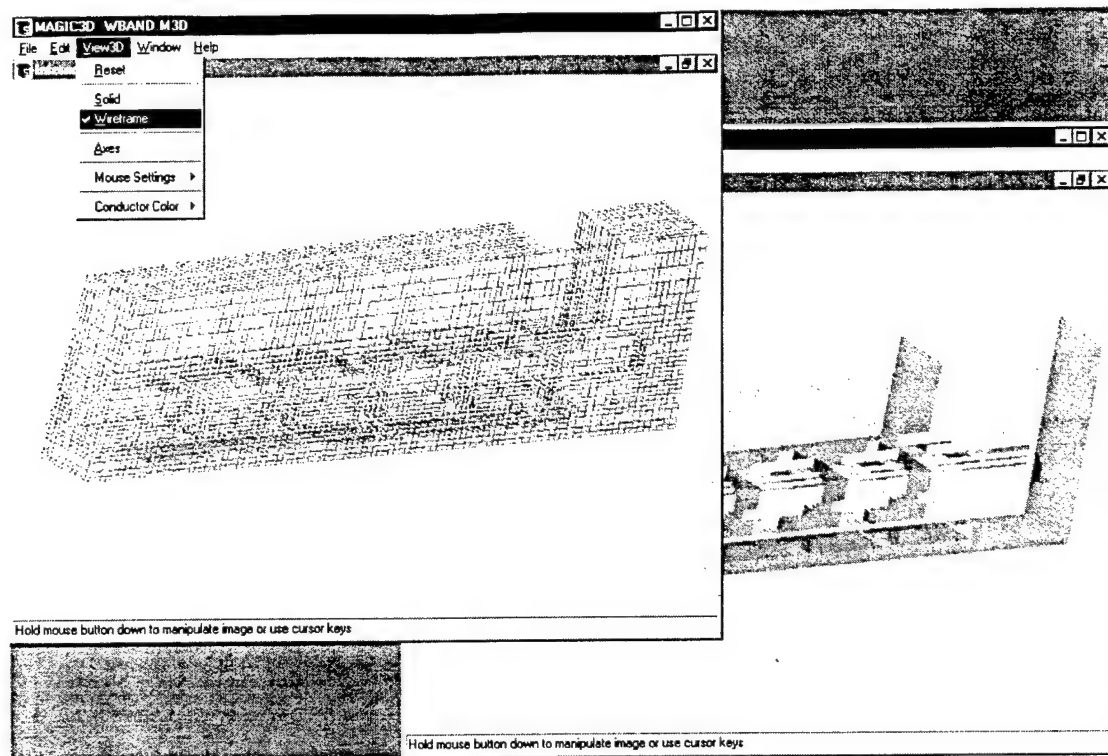
One of the inherent difficulties with 3-D simulation is effectively viewing the geometry. The need for a good viewer goes beyond simply needing good visualization. The MAGIC simulation tool has specific rules about how boundary conditions are to be used, for example, there must be no “holes” in the simulation, e.g., unspecified open boundaries are not permitted. Without the capability to interactively investigate the geometry, as it has been input, it can be difficult to find errors in geometry construction.

During the course of this project, a real-time interactive 3-D viewer was created using OpenGL technology, the inspiration for this work coming from this author’s experience with a popular OpenGL-based PC game, called Bugdom™, which performs real-time geometry manipulation based upon mouse movements, in a manner similar to those desired for simulation. The viewer continues to be upgraded, and is equal to and in some ways superior to most other engineering geometry viewers available. It’s direct incorporation into MAGIC also allows it to be used effectively to check the gridding of the geometry as well.



Cross-section views of a complicated 3-D output cavity for a W-band klystron.

The figures above illustrate cross-sections of a complicated output-cavity, anticipated for use in a W-band klystron at SLAC. The geometry consists of 5 rectangular cavities which are magnetically coupled through slots, instead of through the beam tube, as usual. It is desired to use MAGIC to investigate hot-test frequency shifts, optimum taper, and optimum iris dimensions. The figures below show the same geometry in the interactive 3-D viewer, both as a finite-difference grid, and as semi-transparent material.



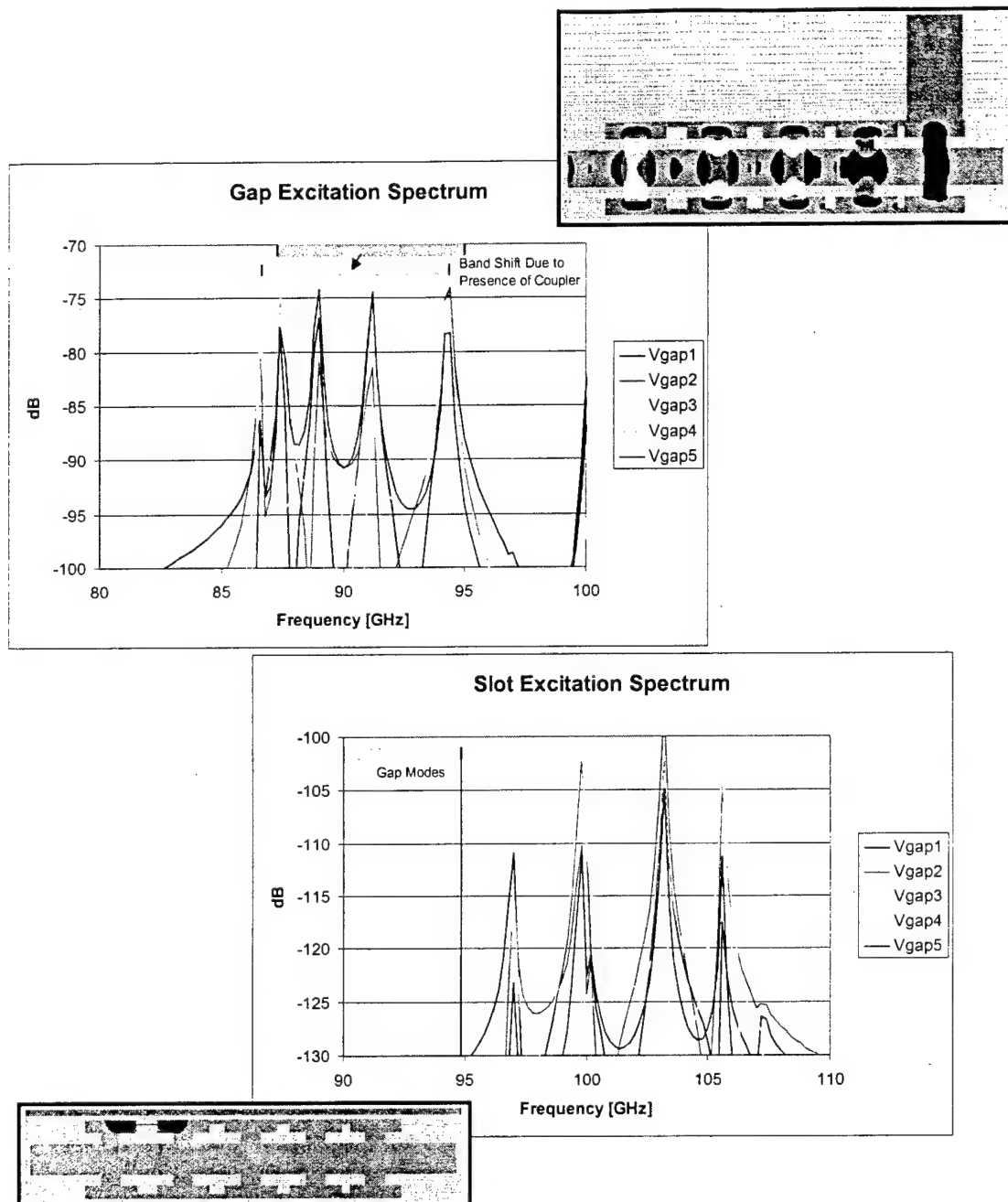
MAGIC's 3-D Interactive viewer of the same W-band structure.

4.3. Full Spectrum Characterization

A multi-cavity structure such as the above usually has several oscillation modes closely spaced, and this collection of modes forms a dispersion relation, which determines how power flows from one cavity to the next. During the past several years, the methodology for determining the entire dispersion relation quickly has progressed markedly.

The primary means of obtaining a complete spectrum of modes is simple, one drives a very fast, very localized, electromagnetic impulse (a “ping”) inside the system, and then lets the system ring. Observations of voltage are made as the system rings. The resultant time history traces look to be an awful mess, but the Fourier transform shows very nice distinct peaks at each of the modes. This technique is not new, however improvements to MAGIC have made it much more practical. These improvements include: a) dB scaling on MAGIC’s FFT plots, b) interactive windowing and zoom on MAGIC’s FFT plots, and c) simplified capability, and published examples, for extracting the spectrum data for easy import into spreadsheets.

An additional capability is the band-selective ping. The location and polarization of the “ping” can favor one set of modes over another. This is especially useful if the structure has several bands that overlap, making the full spectrum difficult to interpret. In the case of the multi-cavity structure from above, there are two low frequency bands, the cavity-gap modes and the slot modes. The two bands do not quite overlap, but are close. There was some concern that tapering the structure would bring the modes into overlap, but simulations show that this does not occur. The figures below show the two bands for this structure.

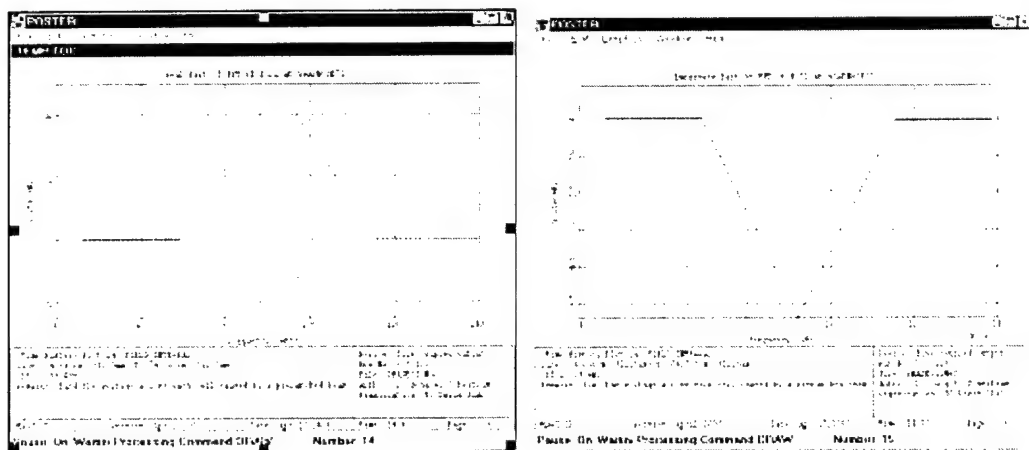


Full-spectrum simulations provide the entire band of modes at once. Careful selection of the “ping” location and polarization can excite just a single band, instead of all modes, which is useful if bands overlap.

4.4. Voltage and Current Phase

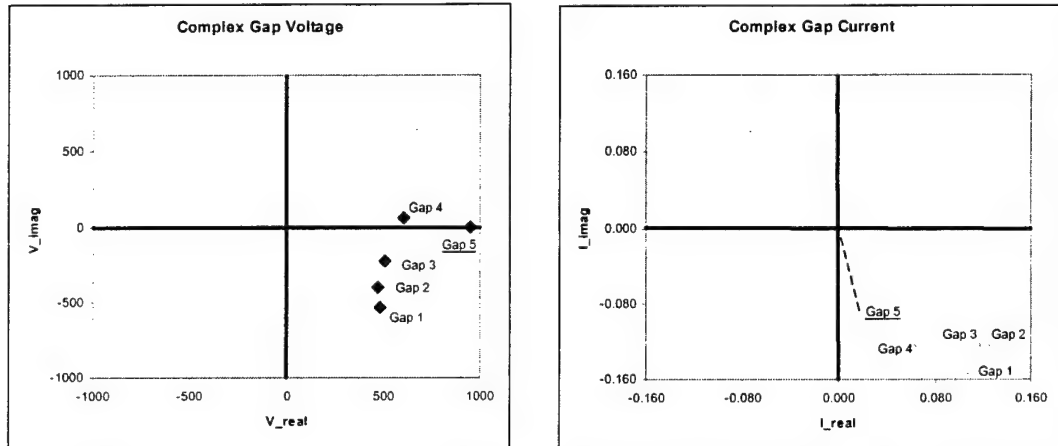
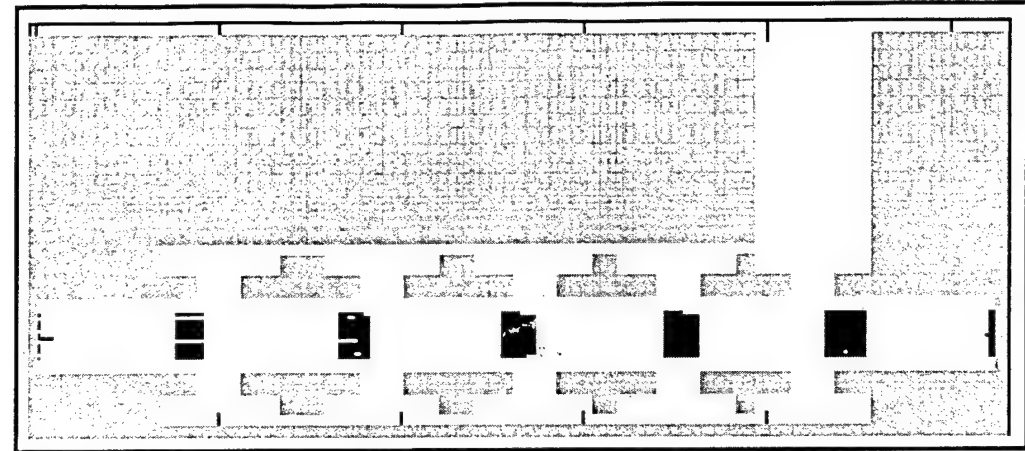
Another issue related to multi-cavity geometry in hot-test is the gap phasing. In cold-test, the gap voltages are typically either in phase or 180° out of phase with each other. The spacing between cavities is determined in order to match the beam current with these voltages. The beam is often losing energy as it traverses the cavity (if it is an output cavity), and the spacing between the cavities must be tapered to preserve uniform transit time from one gap to the next as the beam slows down. Verifying proper phasing between voltage and current in a hot-test situation is one of the most important simulation tasks for multi-cavity geometry. If voltage and current become out of phase, then efficiency is lost.

A method was devised to diagnose this information. The bunched beam is run into the cavity until saturation and CW operation are achieved. Measurement of the gap voltage and mid-gap current is made. A complex FFT of just the last 4-or-so periods is performed, and the time step must be adjusted in this simulation so that the period is an exact multiple of the time step. In this case, there is a sharp triangular peak, as illustrated below, at the drive frequency on the FFT. The real and imaginary value of the peak is plotted on a polar plot, so that there is one point for each cavity. A comparison of voltage with current shows whether any particular gap is not phased in an optimal manner.



Simulation output for voltage and current phase diagnostic.

The 5-cavity output structure previously illustrated provides an example, however for this case, there is no tapering – all cavities are spaced equally. The figures show a pre-bunched beam traversing the structure. The polar plots show the complex voltage and current. Note that the current and voltage in Gap #5 are nearly 90° out of phase, which indicates an average power transfer of nearly zero for this cavity. Bottom line, in this simulation, Cavity #5 is not adding to the output power. This information was further used to help design an efficient taper.



Example of phase diagnostic used to examine current and voltage phasing. Note that the Gap 5 voltage and current are nearly 90° out of phase, leading to less than optimal efficiency for this particular choice of taper.

4.5. Evolution of the RF Current

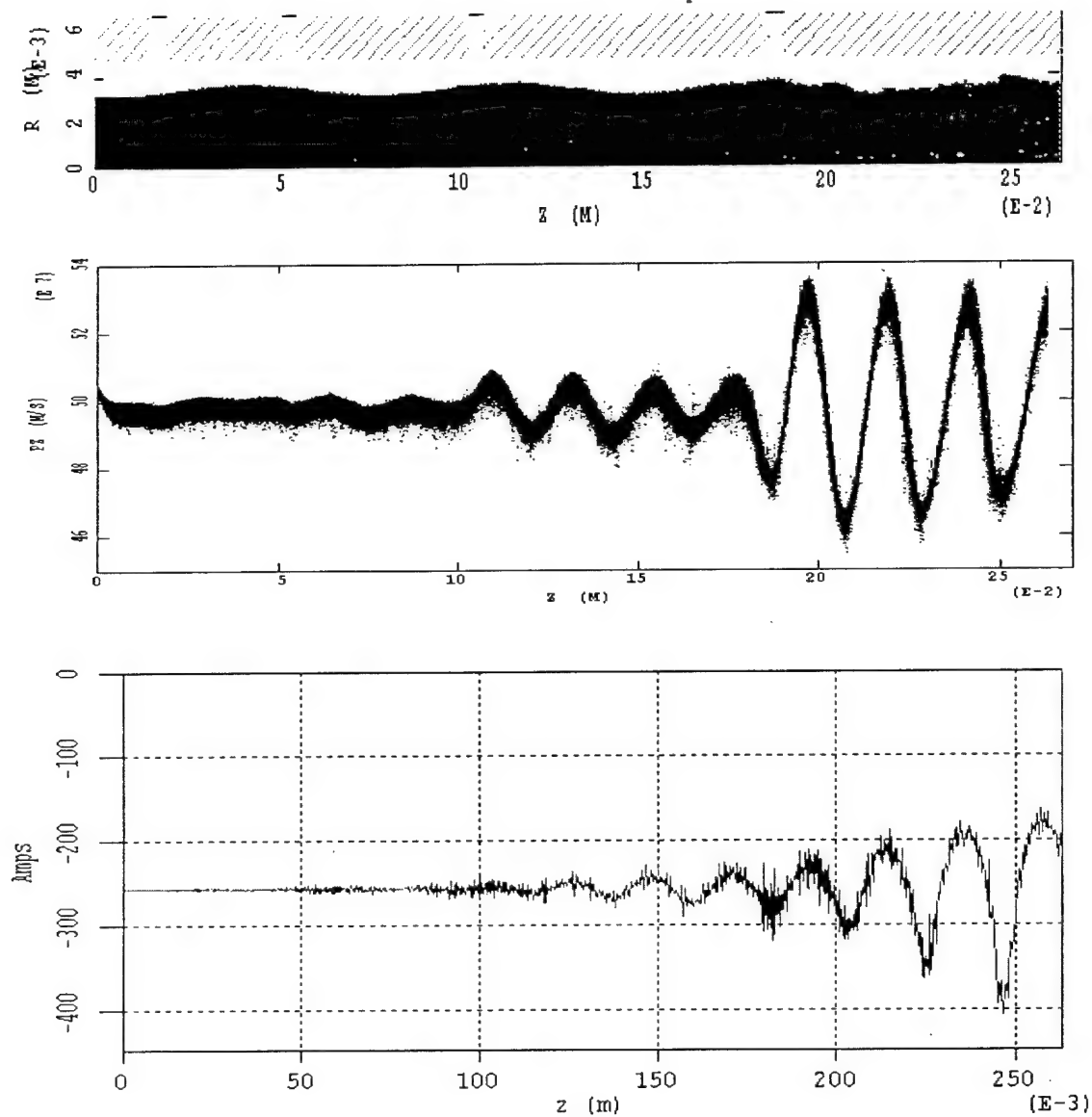
An important new diagnostic developed for this program is the RANGE plot of an RF-component. When one does a spreadsheet design analysis of a klystron, one is concerned with the growth of the RF current as the beam propagates from one cavity to the next. Indeed, the optimal position for the next cavity is usually where the RF current has grown to a maximum. If the drift tube is too long, the RF current actually begins to drop again.

It turns out that this is a fairly difficult quantity to evaluate in a simulation. The particle algorithms provide the current density at each point for the present time-step. From here, this current density must be: 1) integrated across the beam cross-section to get current, 2) multiplied by a complex phase factor, which is oscillating at the known RF frequency, 3) accumulated over one or more cycles, 4) re-normalized and complex

magnitude taken at the end of the cycles, 5) and plotted ... for each point down the axis of the drift tube. These processes were programmed, in order to extract this important quantity.

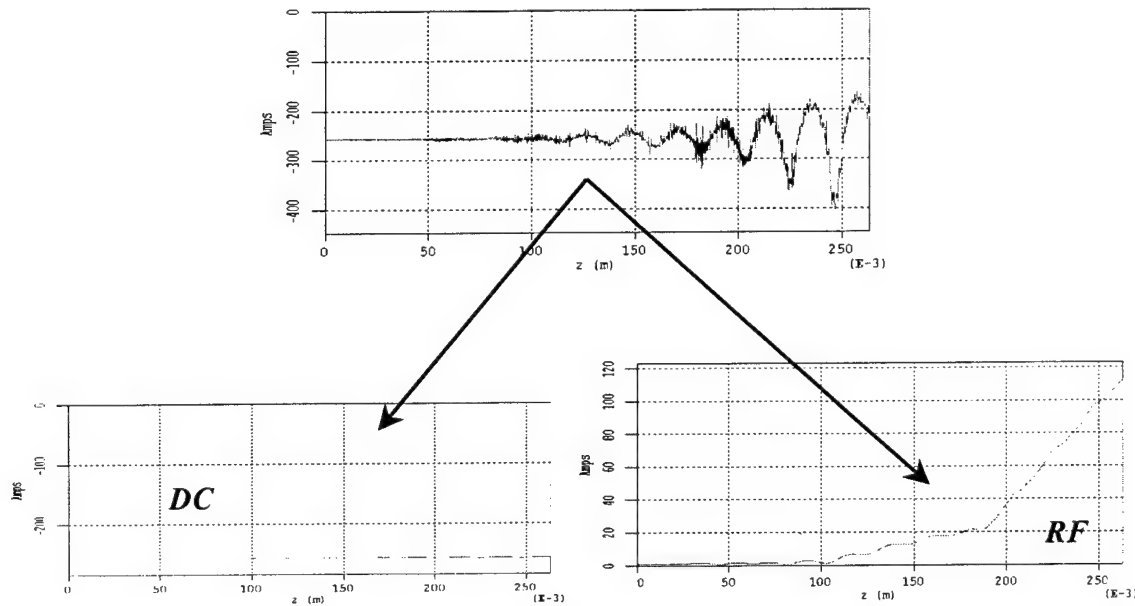
The figure below illustrates the beam in a drift tube with 4 klystron cavity gaps, together with its velocity phase space. The first cavity imparts a very small oscillating signal onto the beam, which is not detectable on the phase space plot, because it is less than the space-charge velocity spread. Nevertheless, this small signal grows, excites the second cavity, which imparts a barely visible velocity modulation, and in turn, until the fourth cavity is now seeing a significant voltage.

An instantaneous snapshot of the beam current down the axis appears as shown below. The bunching finally resulting in visible current modulation after the 3rd and 4th cavities. In fact, the current rapidly acquires strong harmonic content. This makes it difficult to determine what the RF current at the fundamental frequency is.



Four gap klystron simulation showing growth of voltage signal from each cavity, and growth of current modulation as beam propagates down the tube. A diagnostic to quantify the current has been developed.

The new diagnostic solves this problem. In fact, it is possible to separate the DC and RF fundamental currents, as illustrated below. The growth of the RF current is now very nicely illustrated in the third plot.



The new diagnostic can split the current into average DC current and the amplitude of the RF part of the current at the fundamental frequency. This diagnostic also facilitates comparison to analytic design and existing 1-D design codes.

5. New Simulation Models

Two new physics models were added to the MAGIC simulation tool during this project. The first model, surface resistivity, is conceptually simple, and corresponds to the skin-depth penetration of fields into metals, and the subsequent ohmic losses to the metal walls. Nevertheless, implementation of this model requires some care, since the skin depth is usually orders of magnitude smaller than grid cells. Hence a “sub-grid model” is required.

The second model is the Resonant Port model, where an entire klystron cavity is replaced with a boundary condition that mimics its behavior as an equivalent circuit. Not only is this a difficult model to implement, its validity remains under study, despite its long standing use of this approximation in 1-D design analysis.

5.1 Surface Resistivity Along a Metallic Wall

Consider the cell around a magnetic $[\mathbf{H} \cdot d\mathbf{l}]$ element which has a metallic conducting surface of conductivity σ passing through it as shown in the figure below. The magnetic field will result in a surface sheet current, \mathbf{K} . The surface current travels a length dl_K in the cell, and has a cross-section of dw_K times δ , the skin depth, e.g., its resistance is:

$$R_{cell} = dl_K / (\sigma \delta dw_K) = \cos^2 \theta (dl_K dw_K) / (\sigma \delta dl^2) = \cos^2 \theta [R_s dA_{surface} / dl^2] ,$$

where $dA_{surface}$ is the actual metallic surface area within the cell, and $R_s = 1/(\sigma \delta)$ is the standard surface resistivity (units of ohms) which depends only on the type of metal and frequency, and the width of the surface current in the cell is: $dw_K = dl / \cos \theta$, where $\cos \theta = |\mathbf{n}_{surface} \times \mathbf{t}_H|$, the surface normal cross product with the direction of the magnetic field component. The actual surface field is equal to the surface sheet current, is: $K = H_{surface} = H / \cos \theta$, so that the surface current flowing in the cell is:

$$I_{surface} = K dw_K = [\mathbf{H} \cdot d\mathbf{l}] / \cos^2 \theta .$$

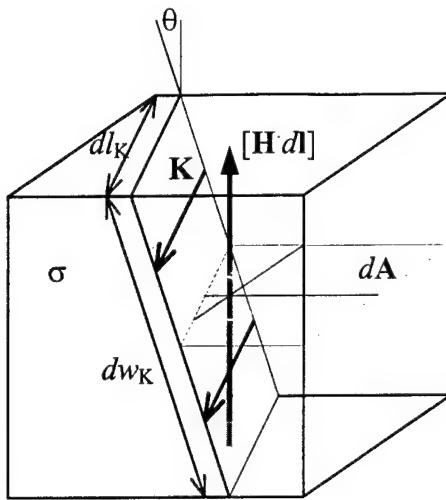


Illustration of a cell containing metal. A proper analysis shows that cosh factors drop out the surface loss terms, resulting in a simple expression to treat skin-depth related ohmic losses.

Ohm's Law gives the voltage across the metallic surface due to the surface sheet current:

$$[V_{ohmic}] = R_{cell} I_{surface} = [\mathbf{H} \cdot d\mathbf{l}] [R_s dA_{surface} / dl^2] .$$

Note that the $\cos\theta$ term drops out, and hence, it is not necessary to be concerned with the angle between the surface and the magnetic field component. The surface voltage enters Faraday's Law as the completion of the loop integral of $\mathbf{E} \cdot d\mathbf{l}$ around the $[\mathbf{B} \cdot d\mathbf{A}/dt]$ element. Hence, for each magnetic field component whose loop integral is interrupted by a resistive surface, introduce the following new field:

$$[V_{ohmic}]^n,$$

which has units of volts, and the following new material quantity:

$$[R_s dA_{surface} / dl^2],$$

which has units of ohms. It will also prove useful to have the following unitless quantity:

$$[\frac{1}{2} \delta dA_{surface} / dl dA],$$

which is essentially the ratio of the skin-depth volume to the cell volume of the field component. Faraday's Law is amended to include the nonzero surface voltage in the loop sum:

$$[\mathbf{B} \cdot d\mathbf{A}/dt]^{n+1/2} = [\mathbf{B} \cdot d\mathbf{A}/dt]^{n-1/2} - \sum_{loop} [\mathbf{E} \cdot d\mathbf{l}]^n - [V_{ohmic}]^n .$$

The surface voltage must be centered on the full time-step, which is achieved with the following time update equation for surface voltage:

$$[V_{ohmic}]^{n+1} = 2 [R_s dA_{surface} / dl^2] [\mathbf{H} \cdot d\mathbf{l}]^{n+1/2} - [V_{ohmic}]^n .$$

The energy damped in a time step is found by evaluating the new $[V_{ohmic}]^n$ term in

$$[\mathbf{H} \cdot d\mathbf{B} dV/dt]^{n+1/2} = 1/2 [\mathbf{H} \cdot d\mathbf{l}]^{n+1/2} ([\mathbf{B} \cdot d\mathbf{A}/dt]^{n+3/2} - [\mathbf{B} \cdot d\mathbf{A}/dt]^{n-1/2}) ,$$

which is:

$$[dP_{surface}]^{n+1/2} = [R_s dA_{surface} / dl^2] ([\mathbf{H} \cdot d\mathbf{l}]^{n+1/2})^2 .$$

Note that this quantity is always positive, indicating damping. This power dissipation formula in differential form is, as expected:

$$\frac{dP_{surface}}{dA_{surface}} = R_s H^2 .$$

A possibly more obvious centering for the ohmic surface voltage, namely

$$[V_{ohmic}]^n = 1/2 [R_s dA_{surface} / dl^2] ([\mathbf{H} \cdot d\mathbf{l}]^{n-1/2} + [\mathbf{H} \cdot d\mathbf{l}]^{n+1/2}) ,$$

results in losses of indeterminate sign in the energy balance equation, and is not recommended. Note that in differential equation form, Faraday's Law for a surface component of \mathbf{B} can be written:

$$\partial_t \mathbf{B} = -\nabla \times \mathbf{E} - \eta \mathbf{B} ,$$

which contains a magnetic damping term, whose coefficient is:

$$\eta = \frac{R_s}{\mu} \frac{dA_{surface}}{dV_{cell}} ,$$

where $dV_{cell} = dA dl$ is the cell volume associated with the surface component.

An important question is the phase of the surface voltage. Up to this point we have assumed that the surface voltage is purely ohmic and is in phase with the surface current. However, it is known from a more exact treatment of skin-depth physics that the surface voltage contains an inductive part which is approximately equal to the resistive part so that the phase of the surface voltage is 45 degrees out of phase with the surface current, e.g., R_s should really be $(1+i)R_s$. This implies the following equation for $[V_{surface}]$:

$$[V_{surface}] = R_{cell} (I_{surface} + (1/\omega) dI_{surface}/dt) , \text{ e.g.,}$$

$$\frac{1}{2}(\mathcal{V}_{surface}^n + \mathcal{V}_{surface}^{n+1}) = [R_s dA_{surface} / dl^2] (\mathbf{H} \cdot d\mathbf{l})^{n+1/2} + (1/2\omega dt)(\mathbf{H} \cdot d\mathbf{l})^{n+3/2} - \mathbf{H} \cdot d\mathbf{l}]^{n-1/2}) .$$

If we use $\mathbf{H} \cdot d\mathbf{l}]^{n+1/2} = [dl dt / \mu dA] [\mathbf{B} \cdot d\mathbf{A}/dt]^{n+1/2}$, and note that $R_s/\omega\mu=\delta/2$, and use a $[V_{ohmic}]^n$ which satisfies the previous rule for just the ohmic effects, then the surface voltage becomes the following:

$$[\mathcal{V}_{surface}]^n = [V_{ohmic}]^n + [\frac{1}{2} \delta dA_{surface} / dl dA] (\mathbf{B} \cdot d\mathbf{A}/dt)^{n+1/2} - [\mathbf{B} \cdot d\mathbf{A}/dt]^{n-1/2}) .$$

When this surface voltage is plugged into Faraday's Law, the result is the same as before,

$$[\mathbf{B} \cdot d\mathbf{A} / dt]^{n+1/2} = [\mathbf{B} \cdot d\mathbf{A} / dt]^{n-1/2} - \sum_{loop} [\mathbf{E} \cdot d\mathbf{l}]^n - [V_{ohmic}]^n ,$$

except that the new area element of the magnetic field is

$$d\mathbf{A} = d\mathbf{A} (1 + [\frac{1}{2} \delta dA_{surface} / dl dA]) .$$

A simple way to interpret this is that the active volume for the magnetic field component increases by exactly $\frac{1}{2} \delta dA_{surface}$ to account for the inductive effect of the skin-depth.

Another important question for the surface resistivity loss is the preservation of the $\nabla \cdot \mathbf{B}=0$ relation, since it is Faraday's Law which guarantees this. In fact, the formulas written above will introduce an apparent error in $\nabla \cdot \mathbf{B}=0$ evaluated at the cell center. However, it will be quickly realized that this error is actually an expression of the small normal magnetic field, which must exist in conjunction with a nonzero $V_{surface}$. In fact, the divergence condition may be used to derive the value of this small normal magnetic field.

5.2. The Resonant Port Model

During this project, the “Resonant Port Model” was conceived, implemented, improved, and studied. This work can be qualified as falling under the original proposal section of a 1-D cavity optimization tool (#2.2.6). There is tremendous desire is for a “quick analysis” tool which can perform an entire klystron analysis in a sort amount of time, say 2 hours or less. Several such tools already exist and are in use at SLAC. Many of these tools take only minutes to run. There was no desire to replicate that which already exists, rather it was desired to provide capability which did not exist, or did not function reliably. In the end, such a tool has been constructed. However, ironically, having now a better understanding of the compromises necessary for doing such quick analysis, the desire to perform full physics analysis seems stronger.

For klystrons, proper tuning of the cavities is of utmost importance. While seemingly a straight-forward task, the precision with which the klystron cavities must be tuned far exceeds the precision necessary to adequately simulate other cavity devices, such as coupled cavity TWT’s. In general, cavities must be frequency tuned to within 1% for a semblance of proper behavior, and 0.1% for accurate performance prediction, e.g., for accurate power and bandwidth. In a typical time-domain simulation of a klystron cavity, most of the simulation time is spent in filling the high-Q cavities, e.g., it requires 100 RF cycles to fill a single cavity, and 1000 RF cycles to bring a multi-cavity simulation to a CW state.

Tuning cavities in MAGIC is simple enough using the eigenmode algorithm. However, one must also tune the Q of the cavity, which requires a time-domain ring-up-to-CW simulation. And naturally, the coupler or loss-element can de-tune the eigenmode slightly, so that iteration is required. Many eigenmode solvers, but not MAGIC, perform *complex* eigenmode solutions, so that the frequency and Q can be simultaneously tuned. This works reasonably well for high-Q buncher cavities, however it can be dangerous for low-Q cavities, such as the output cavity. If not done properly, the complex eigenmode results in the ring-down field pattern. If the coupler or loss-element is small and localized, the ring-down field pattern can be significantly different from the CW field pattern. Thus it is always a good idea to test an output cavity by simulating its CW field pattern in a time-domain simulation.

Then finally, the last insult to the tuning task is the fact that the presence of the beam alters the frequency of the cavity. This is easy to visualize if one recalls the RLC circuit representation of a cavity. The capacitance, C, is simply the voltage gap between the re-entrant noses of the cavity, and the inductance, L, is simply the volume of the cavity, filled with magnetic field. The beam inserts a plasma into the space of the capacitor, thus changing the effective dielectric constant of the capacitor, thus changing the capacitance, and thus finally changing the frequency of the RLC circuit. The change in frequency can be on the order of 0.1%, even more for a high perveance beam such as an MBK, and thus, if not properly accounted for, can result in improper prediction of power and bandwidth. Thus, there must be iteration on the cavity tuning during hot-test as well. One of the very unpleasant discoveries of this effort is that this beam-loading-

induced frequency-shift changes sign when the drift tube grows larger relative to the cavity radius, as is the case for most higher frequency designs now on the drawing boards. Thus, a great deal of the experience and intuition which has evolved over the past decades to deal with this issue is, in fact, not applicable at the higher frequencies.

To date, the effort spent on the Resonant Port Model has not resulted in the desired “quick analysis tool”, although it potentially could. In the end, we have learned a great deal about why the existing fast design tools sometimes appear to work and sometimes don’t, and why quickness may involve uncertainty. This improved understanding of what is happening in existing tools has been useful in its own right to SLAC personnel. But it is not safe to say that what has been implemented to date has been adopted and is being used as a design tool. Part of the difficulty lies in the success of full-blown 2-D simulation. The “fast design” version of a klystron in MAGIC must compete with an outright full-blown simulation with complete physics. In the end, the full-blown MAGIC seems to have won out over a “quick analysis” MAGIC ! Computers get faster, and what was once a long run soon becomes commonplace, and quick is not so quick if afterwards you then have to spend days fretting over known uncertainties. Having said this, note that it applies to 2-D simulations of conventional klystrons at SLAC, there still may be considerable need for a 3-D quick analysis tool in MAGIC.

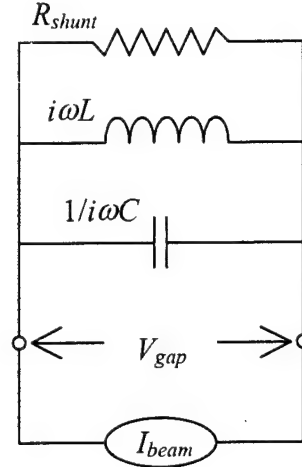
The quickest design analysis tools are 1-D, and simply push electrons through oscillating voltages representing the cavities. The response of the cavity is based on an RLC circuit model, and the beam current driving this circuit is collected using the so-called Ramo’s Theorem, e.g., the current density is weighted with the electric field profile seen by the beam in the cavity gap. Such 1-D design tools exist in profusion and some of them function quite satisfactorily. A 2-D improvement of this is possible using the so-call “Port Approximation”, the beam propagates in a 2-D drift tube, the cavity is omitted, and instead a forced voltage is applied at the location of the cavity gap. The voltage is constructed from the same RLC circuit model as the 1-D model, one simply uses the 2-D version of Ramo’s Theorem to construct the current.

Why does one desire a 2-D generalization? Three reasons are manifest: 1) profile effects, for example, typically the center of the beam sees a slightly larger voltage, but it is spread out more, thus having a weaker coupling coefficient (these two effects offset each other), 2) inclusion of the magnetic field and beam optics, especially in the case of PPM focusing, and 3) inclusion of beam space charge effects. Previous work on “Port Approximations” has been made, and while some of it appears to be very promising, in actual design practice, the ultimate confidence in this method is often less than the 1-D method, as results have sometimes strayed far from the sensible.

Clearly, then, the 2-D “Port Approximation” is the starting point for this work, and indeed the “Resonant Port Model” is a “Port Approximation” in the manner in which it has been described so far. By way of review, MAGIC’s RESONANT_PORT model applies a forced-voltage at some boundary along the drift tube, where the gap of a cavity would normally be. This is subtly but significantly different from previous fixed-mode port-models, which enforces not just the driving voltage, but the entire mode-pattern of

the cavity eigenmode everywhere inside the drift tube. By contrast, in the MAGIC simulation, only the boundary field is fixed, everywhere else the eigenmode must form self-consistently via time-domain Maxwell-equation propagation and reinforcement.

The voltage response, in either case, is based upon the circuit illustrated below.



Equivalent circuit for a klystron cavity, used in most port-approximations.

A simple circuit analysis shows that the relationship between I_{beam} and V_{gap} , written in terms of the cavity impedance is:

$$Z_{cavity} = \frac{V_{gap}}{I_{beam}} = \frac{1}{i\omega C + \frac{1}{i\omega L} + \frac{1}{R_{shunt}}} = Q \left(\frac{R_{shunt}/Q}{1 + \Delta(\omega)} \right)^{1-i\Delta(\omega)},$$

where:

$$\Delta(\omega) \equiv Q \left(\frac{\omega}{\omega_0} - \frac{\omega_0}{\omega} \right) \approx 2Q \frac{\delta\omega}{\omega_0},$$

and the fundamental cavity parameters are:

$$Q,$$

$$\omega_0 \equiv (LC)^{-1/2}, \text{ and}$$

$$(R_{shunt}/Q) \equiv (L/C)^{1/2}.$$

Note that for fixed current, and varying frequency, the peak impedance (peak voltage) occurs when $\omega=\omega_0$, and that at this frequency voltage and current are in phase, and the

impedance is exactly R_{shunt} . Note that the parameter (R_{shunt}/Q) represents the stored energy of the cavity, and despite the unfortunate nomenclature, it has little to do with the Q parameter, which represents the coupler or loss-element in the cavity.

The circuit is driven by the beam-current, I_{beam} , which is found from Ramo's Theorem, according to:

$$I_{beam} \equiv \int_{gap_region} d^3r \mathbf{J}(\mathbf{r}) \cdot \mathbf{E}_{mode}(\mathbf{r}) ,$$

where $\mathbf{J}(\mathbf{r})$ is the particle current density and $\mathbf{E}_{mode}(\mathbf{r})$ is the resonator eigenmode fields normalized for unit voltage across volt_line. This is, in fact, the basis of the original BEAM_CURRENT algorithm.

It can be seen that in a typical fixed-mode port-model, the product of I_{beam} and gap-voltage, V_{gap} , is exactly identical to the $\mathbf{E} \cdot \mathbf{J}$ energy transfer between cavity and beam, by virtue of the fact that the \mathbf{E} fields are fixed to be exactly \mathbf{E}_{mode} . Thus, energy transfer is the same, whether you look at it from the cavity perspective, $I_{beam} \times V_{gap}$ or the field perspective, $\mathbf{E} \cdot \mathbf{J}$.

But in the MAGIC implementation, the \mathbf{E} fields are fixed to be \mathbf{E}_{mode} only at the boundary, everywhere else they must establish themselves consistent with Maxwell's equations. Not surprising then, differences between the power from the cavity perspective, $I_{beam} \times V_{gap}$, and the power from the field perspective, $\mathbf{E} \cdot \mathbf{J}$, can emerge. Such differences have been demonstrated to occur as one might reasonably expect, when:

- a) a poor quality approximation of \mathbf{E}_{mode} is used, or
- b) the drive is off-center-frequency, and \mathbf{E}_{mode} is the center-frequency mode pattern.

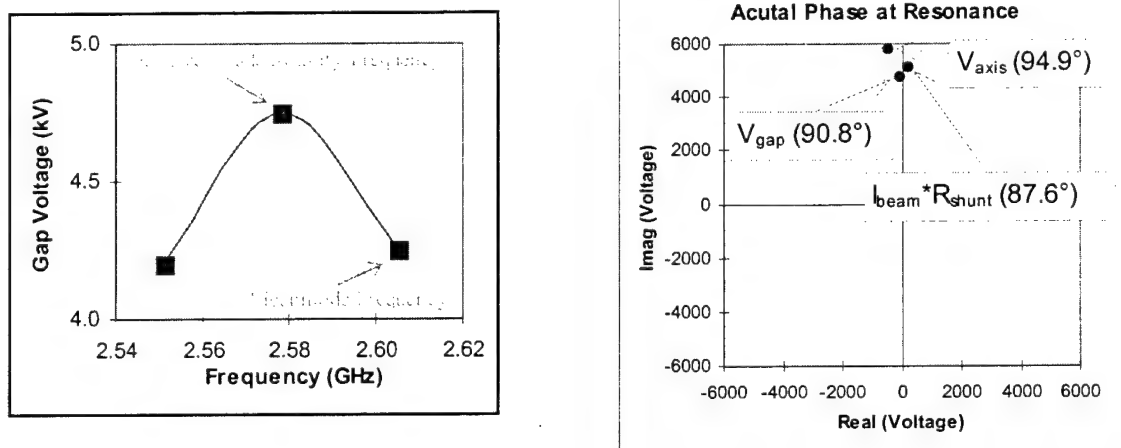
An example is very illustrative here. Suppose that we perform a full-physics, full-cavity simulation and diagnose the gap voltage and the Ramo's theorem current. We select a fairly challenging test case, where the cavity parameters are very carefully diagnosed to be: $Q = 27.3$, $R_{shunt}/Q = 71.3 \Omega$, $\omega_0 = 2\pi(2.578 \text{ GHz})$, and gap length = 1 cm. The beam parameters are also fairly challenging, 30 kV, 12.5 amps, with 5.4 amps AC; and the beam is confined with a strong uniform magnetic field. This represents a high perveance (2.4) and a reasonable transit angle (90 degrees). We still confine ourselves to small signal, though ($V_{gap} \ll V_{beam}$). The results are impressive when everything is done right, e.g., when we use the exact cold-test eigenmode fields, \mathbf{E}_{mode} , for diagnosing the Ramo's Theorem induced current.

The example simulation is repeated several times at several different frequencies. In this example the loss-element results in a frequency downshift shift of about 1% from the eigenmode value, see the figure below. There is almost no frequency shift due to the presence of the beam in this run. And indeed, the maximum gap voltage, 4.75 kV, occurs at the loaded-cold-test frequency. The Ramo's Theorem induced current is computed as a diagnostic and has a magnitude of **2.42 amps**. Based on the circuit model, we would have expected a current of:

$$I_{beam} = V_{gap} / (R_{shunt}/Q) / Q = (4.75\text{kV}) / (71.3\Omega) / (27.3) = 2.44 \text{ amps.}$$

This would appear to be very good agreement, and a confirmation that the circuit model can be used to successfully represent a cavity. Note that the Ramo's Theorem current, 2.42 amps is not the same as the known AC current, 5.4 amps, because of gap transit time effects. The Ramo's Theorem calculation automatically accounts for this effect, commonly known as the beam's "coupling coefficient".

Let us now take a closer look at the current and voltage phasing in the run exactly at resonance. Recall that the current and voltage are expected to be in-phase at this point. The figure below shows three measurements of voltage in the complex plane. All three are clustered close together at a phasing of about 90°. The measurements are the voltage on axis, V_{axis} , the voltage at the gap, V_{gap} , and the equivalent circuit voltage based on the Ramo's Theorem current and the known circuit impedance, $I_{beam}R_{shunt}$. The gap voltage is expected to be slightly smaller in magnitude than on axis, however note that it also contains a 4.1° phase shift. The equivalent circuit voltage contains a further shift of 3.2°, for a total shift between axis voltage and circuit voltage of 7.3°. All three voltages are expected to have identical phase. If a phase shift of this size were to occur in the circuit model, it would be attributable to having the frequency 0.25% off resonance, which is about half a division in the figure below, and would be quite noticeable in terms of reduced voltage. Thus, some other effect is at the origin of the phase shift.



Center frequency of an actual cavity, together with a comparison of the complex gap voltage and beam current. The fact that there is some noticeable phase shift between the voltages and the current indicates that there are physics issues which is not modeled by the traditional port models. Beam space charge is one such issue.

One likely candidate is space charge effects. The phase difference between axis and gap voltage might seem to favor this interpretation. The space-charge field is ignored in the circuit model. Likewise, in the usual 1-D and many 2-D port approximations, the particle momentum are updated with a Lorentz force based on just

the circuit voltage and the electric field of the eigenmode field profile; the electric field of the beam's space charge is not included.

One of the reasons that the circuit model and Ramo's Theorem current have worked reasonably well without the space charge fields of the beam is that the space charge fields are typically about 90° out-of phase from the beam current. This is illustrated in the following figure, the space charge fields are zero at the center of a bunch, where the current is maximum. Thus, even when the space-charge fields are not negligible in magnitude, their $\mathbf{E} \cdot \mathbf{J}$ product averages to nearly zero over a cycle, so that there is little or no energy transfer associated with these fields.

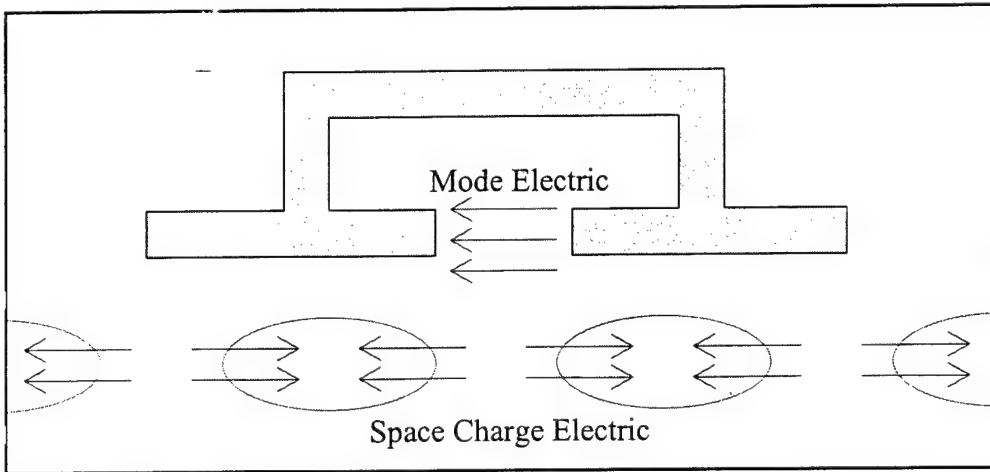


Illustration of why beam space charge has little or no effect at center frequency. Space charge and mode fields are 90° apart in phase. Understanding this figure, one can then realize why off-center driven cavities, such as used in stagger-tuning, are more likely to show anomalous behavior related to space charge effects.

Examination of the off-resonance cases of our example shows markedly larger error than for the on-resonance case that we've just looked at. And indeed, off-resonance, such as what might occur with a stagger-tuned klystron, is where one would like to have better design capability. Generally speaking, there are two situations in which the 2-D port models are known to produce unsatisfactory results. First is if the mode patterns are not accurate – this makes perfect sense, because inaccurate mode patterns will lead to, at the very least, an improper coupling coefficient. Second is if the cavity is not operating close to center-frequency – this second situation sometimes leading to difficulty and sometimes not. However, now we can see that if the cavity is operated off center-frequency, then the cavity voltage will not be exactly in-phase with the current, and hence will not be exactly out-of-phase with the space charge fields. E.g., the space charge fields will now be able to add or subtract from the cavity mode fields, and can no longer be ignored so far as their contribution to the Lorentz force.

Upon realization of this situation, it was decided that MAGIC could be made to operate in a manner that encompassed the equivalent circuit model, with a port-approximation, and at the same time still treat space charge effects. Such a treatment would indeed represent progress from what has been done in the past. MAGIC simply applies the circuit voltage as a boundary condition along the line of the port, rather than

everywhere inside the drift tube. The fields inside the tube are computed from Maxwell's equations in the usual manner, thus including space-charge effects.

This scheme worked well so long as one was operating exactly at center-frequency, and so long as the Ramo's Theorem field profiles were very good approximations of the actual fields. If either of these conditions were not satisfied, the result was an appalling failure, often with the beam gaining net energy from its interaction with the cavity ! The reason for this failure to conserve energy is fairly simple to understand. We are no longer forcing \mathbf{E} to be exactly \mathbf{E}_{mode} in the presence of the beam, so the energy product, $\mathbf{E} \cdot \mathbf{J}$, is not necessarily equal to $\mathbf{E}_{mode} \cdot \mathbf{J}$, which is the assumption of the circuit model driving the boundary condition. Thus we are made even more aware of the significance of the space charge fields within the beam.

The solution to this problem was to drive the circuit with the so-called "gap-current", I_{gap} , which is computed from the magnetic field at the boundary, e.g., using the poynting-power product $\mathbf{E}_{mode} \times \mathbf{H}$, instead of the mechanical-power, $\mathbf{E}_{mode} \cdot \mathbf{J}$, which is the basis of Ramo's Theorem. It is officially defined to be

$$I_{gap} \equiv \oint_{boundary} d\mathbf{A} \cdot [\tilde{\mathbf{E}}_{mode}(\mathbf{r}) \times \mathbf{H}(\mathbf{r})]$$

Now since \mathbf{E} is fixed to be \mathbf{E}_{mode} right on the boundary, we are back to a situation of having the power in the cavity perspective, $I_{gap} \times V_{gap}$ equal to the power in the field perspective, $\mathbf{E} \times \mathbf{H}$. But, unfortunately, we have now introduced new uncertainty, as to the physical meaning of I_{gap} , and how it is to be used in a circuit that was designed for I_{beam} , not I_{gap} .

The simplest escape from this uncertainty is to establish a sensible relationship between I_{gap} and I_{beam} , so that we can continue to use the existing circuit. To do this, let us consider that the RESONANT_PORT boundary condition is typically applied at the noses of the cavity, and that the stored electric field energy, e.g., the "capacitance", of the eigenmode is concentrated primarily in the drift tube, and in the field concentrations around the noses. In other words, the RESONANT_PORT boundary splits the circuit capacitor into two parts, that part which is modeled by the boundary condition, and that part which is modeled by self-consistent Maxwell field evolution. This "split-capacitor" is illustrated in the following figure. It is also asserted that the proper physical interpretation of the so-called gap-current, I_{gap} , is simply that it is the transformation of the beam current, I_{beam} , through the part of the split-capacitance that is modeled by the self-consistent Maxwell field evolution.

The capacitance splitting parameter is κ_C , which represents the fraction of the capacitance treated by the boundary condition. The GAP_CURRENT algorithm simply uses the upper portion of this circuit, above the V_{gap} nodes, replacing the original capacitance with $\kappa_C C$, and driving the circuit with the computed gap current. The difficulty with this, in practice, is that a very accurate estimate of κ_C is required. In addition, it was found that this circuit model did not rise up to CW as fast as the Ramo's Theorem current model typically does.

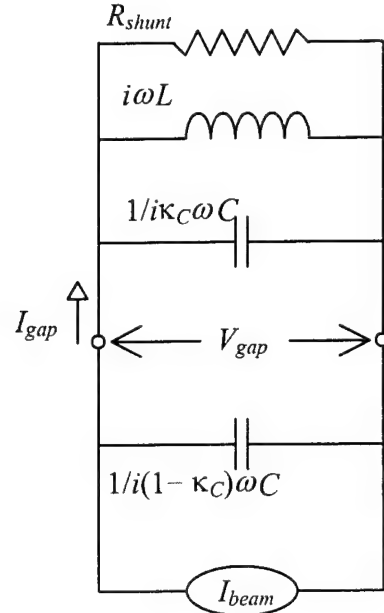


Illustration of the equivalent circuit for a klystron cavity in MAGIC's Resonant Port approximation. The capacitance is split, with the part in the drift tube treated self-consistently via Maxwell's equations, and the part in the cavity treated by the boundary condition.

The resonant port boundary condition underwent two important changes during the year 2000. The first change was a narrow-banding of the current-input to the model, around the specified frequency. The second change was the addition of a new current algorithm, called the MIXED_CURRENT option. This is also now the default algorithm for RESONANT_PORT. These two fixes remove:

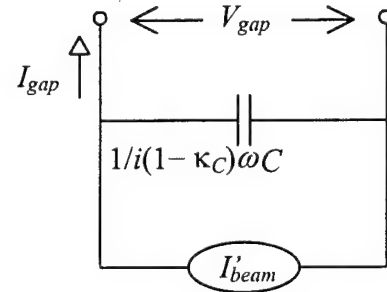
- 1) the energy-conservation problem of the old BEAM_CURRENT algorithm,
- 2) the slow-saturation problem of the old GAP_CURRENT algorithm,
- 3) the need for hyper-accurate estimates of modeled-capacitance fraction, and
- 4) the need for hyper-accurate eigenmode patterns.

The new MIXED_CURRENT option may be interpreted as either the GAP_CURRENT model, together with a dynamic estimate of the modeled-capacitance fraction, or as the BEAM_CURRENT model, with a correction on the beam current to insure energy conservation.

The new MIXED_CURRENT algorithm performs an equivalent operation, except that it transforms the computed gap current back to an equivalent beam current, I'_{beam} , and then uses that in the original circuit, instead of the actual beam current. This simple transformation is:

$$I'_{beam} = I_{gap} - (1-\kappa_C)C \frac{dV_{gap}}{dt} ,$$

as represented in the illustration below.



The advantage of using the gap current in this manner is that this equivalent beam current, I'_{beam} , can be compared to the computed beam current, I_{beam} , and this comparison can be used to validate and improve on the split capacitance, $(1-\kappa_C)C$, and illustrate the difference between I_{beam} and I'_{beam} .

Solve this same equation for the split capacitance, employing the actual beam current, I_{beam} . Then, in order to enforce a pure real capacitance, dot this with the conjugate of dV_{gap}/dt , and take the real part.

$$(1 - \kappa_C)C = \frac{\operatorname{Re} \left\{ \left(\frac{dV_{gap}}{dt} \right)^* (I_{gap} - I_{beam}) \right\}}{\left| \frac{dV_{gap}}{dt} \right|^2} .$$

Thus, the difference ($I_{gap} - I_{beam}$), compared to dV_{gap}/dt , provides a direct evaluation of the split capacitance. When this capacitance is used, the equivalent beam current and actual beam current are related according to

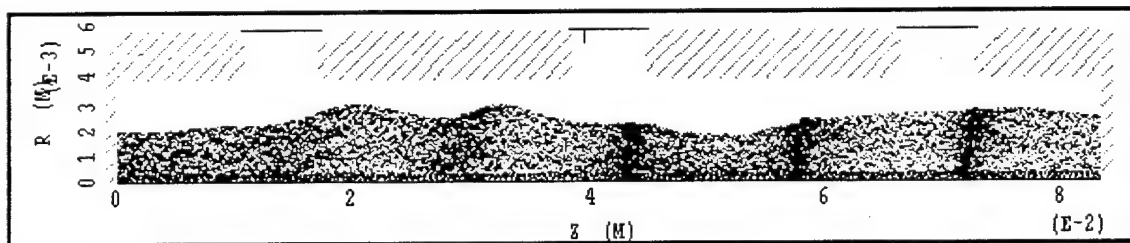
$$I'_{beam} = I_{beam} + i \frac{\text{Im} \left\{ \left(\frac{dV_{gap}}{dt} \right)^* (I_{gap} - I_{beam}) \right\}}{\left(\frac{dV_{gap}}{dt} \right)^*}$$

Thus, the MIXED_CURRENT algorithm is equivalent to using the beam current, together with a correction term, involving the gap current, which insures energy conservation. When the difference between I_{gap} and I_{beam} is purely reactive, e.g., as it would be for the transformation of current through a capacitance, then the correction term is zero.

Finally, it must be said that, in actuality, both the capacitor and inductance are split in the circuit representation, which complicates the math somewhat. However ultimately, one can recast this as a split reactance, which will ultimately be capacitive in nature, and thus appear much as described here.

This final form of the RESONANT_PORT model was completed near the end of the project. There is now underway an attempt to use this improved version for design purposes, but it is too soon to tell what the final outcome will be, and whether use of the RESONANT_PORT model is any quicker, in the end, than just simulating the entire cavity. It is, after all, difficult to compete with an established method which includes space-charge, beam dynamics, harmonics, e.g., nearly all the physics one could desire, even if that method is supposedly slow.

The figure below shows a simulation with three RESONANT_PORT boundaries representing three cavities. The progression of the bunching is quite visible.



Three cavity klystron simulated with the Resonant Port model.

6. A Future Model, Smooth Boundary Modeling

MRC is pursuing a partial-cell-elements boundary condition that will be able to model smooth conducting surfaces without the usual stair-stepped boundary. This effort is funded primarily through an alternate research contract, F49620-00-C-0012, which is focused on aspects of computation plasma physics. However, of all known applications for computational plasma physics tools, the klystron is one which will benefit from such capability the most, and examples from this project provide to this effort the best test of its capabilities. This has become manifestly apparent in working with the various design efforts at SLAC, during the course of this contract.

The mathematical underpinnings of the partial-cell-elements boundary condition, were presented at the 1998 MAGIC User's Group Meeting. Klystron examples, including some from SLAC, were the main motivating examples for this talk. The talk has been published on the MAGIC User's Group Website, since then. However, it has never been formally published elsewhere. This fact is remedied in the following pages. Further discussion of specific details of how this boundary relates to the klystron follow.

Particle-in-cell simulation of klystrons is difficult for the simple reason that the cavities must be tuned to usually 4 decimal places, sometimes 5, primarily because of Q's on the order of several 100's. However, typically, the number of grid cells, in any one dimension, used to model the cavity can be anywhere from 20 to 100 cells. Thus, having an outer radial boundary which is uncertain by $\frac{1}{2}$ a cell can result in a frequency shift in the 3rd decimal place, which is enough to completely de-tune the cavity and render the simulation hopelessly inaccurate. In addition, the stair-stepped boundaries also introduce uncertain cavity shape and volume, which can affect both the tune, and the close-to-wall field profiles.

When one is simulating a single cavity, this is not a problem, one simply assures (MARK's in simulation syntax) that there is a grid line exactly at the proper radius. However, if there are several cavities with very slight differences in radius, and indeed, this is exactly the case for most klystrons, then it is impossible to have grid lines at all the radii, because they all fall in a distance smaller than a grid cell. Going to smaller grid cells is unacceptable because of the severe increase in CPU time.

In MAGIC 2-D, we have adopted the SHIM sub-grid model to treat this condition. SHIM effectively adds partial cells of metal, and is quite successful at addressing the problem. However it is unwieldy to use, easy to mis-use, and prone to errors in diagnostics and modeling when not used "just-so". In MAGIC 3-D, the problem is worse yet. There is no SHIM model, as yet, and so the user must add individual cells, by hand, and tune by trial and error. Add to this fact that, in 3-D, one is almost always desperate to use as few cells as possible to reduce CPU time, so that cavities are coarsely resolved (e.g., 20 cells instead of 100), and the stair-stepping and boundary conflict is exacerbated by the large cell size.

This problem has been recognized for a long time, and a generalized and user-friendly partial-cells algorithm has been devised over the past several years, and is in the early stages of implementation. The foundation of the algorithm is a particular manner of expressing the finite-difference equations used in the MAGIC tool, which provides an exact finite-difference version of the Poynting theorem. The concept of discontinuity operators is used to encompass the partial-cells method. Some detail of this is outlined below. This is augmented by duplicates of the slides used to describe the partial-cells algorithm at the MAGIC User's Group Meeting.

6.1 Extrinsic-Finite-Difference

The spatially gridded unknowns are the fields:

$$\begin{aligned} & [\mathbf{E} \cdot d\mathbf{l}]^n, \\ & [\mathbf{D} \cdot d\mathbf{A}/dt]^n, \\ & [\mathbf{H} \cdot d\mathbf{l}]^{n+1/2}, \text{ and} \\ & [\mathbf{B} \cdot d\mathbf{A}/dt]^{n+1/2}. \end{aligned}$$

They have units of volts, amps, amps, and volts, respectively. Physically, they represent the voltage between two points of the electric field, the instantaneous displacement current of the electric field, the enclosed current of the magnetic field and the instantaneous emf of the magnetic field. All electromagnetic fields are order one in finite-difference deltas. The spatially gridded source current and charge,

$$\begin{aligned} & [\mathbf{J} \cdot d\mathbf{A}]^{n+1/2}, \text{ and} \\ & [\rho dV/dt]^n, \end{aligned}$$

both have units of amps and are order two in finite-difference deltas. The current is co-located with the **E** and **D** fields, while the charge is located at the cell corners.

The finite difference form of Maxwell's curl equations using these fields is:

$$\begin{aligned} [\mathbf{B} \cdot d\mathbf{A}/dt]^{n+1/2} &= [\mathbf{B} \cdot d\mathbf{A}/dt]^{n-1/2} - \sum_{loop} [\mathbf{E} \cdot d\mathbf{l}]^n, \text{ and} \\ [\mathbf{D} \cdot d\mathbf{A}/dt]^{n+1} &= [\mathbf{D} \cdot d\mathbf{A}/dt]^n - [\mathbf{J} \cdot d\mathbf{A}]^{n+1/2} + \sum_{loop} [\mathbf{H} \cdot d\mathbf{l}]^{n+1/2}, \end{aligned}$$

These two equations comprise the leap-frog field update algorithm. Notice that only addition and subtraction are used, no multiplication or division is performed in these curl equations. The beauty of the extrinsic difference formulation is that all finite difference deltas are absorbed into the field and material quantities, and are not needed as independant quantities, except for diagnostic output. Furthermore, it can be further demonstrated that the particle algorithms naturally give current and charge in the above form, and naturally require the **E** and **B** fields for the Lorentz force in the above forms.

The Maxwell divergence equations are:

$$\sum_{star} [\mathbf{B} \cdot d\mathbf{A}/dt]^{-1/2} = 0 \text{ , and}$$

$$\sum_{star} [\mathbf{D} \cdot d\mathbf{A}/dt]^0 = [\rho dV/dt]^0 .$$

These equations serve as initial conditions.

6.2 Poynting's Theorem and Poynting Flux

The finite-difference equivalent to the Poynting flux, $\mathbf{E} \times \mathbf{H}$, cannot be easily assigned to a specific location on the grid, because the electric and magnetic fields are not co-located. It is truly an extrinsic quantity; its very definition requires the specification of a control volume extending over several cells. Once the control volume is specified, though, Poynting's theorem is easily constructed in the usual manner. First, though it will simplify the mathematics somewhat if we introduce a simple differencing function. The existence of this differencing function also serves to illustrate the important property of reciprocity between the E-curl-loops and B-curl loops. Any finite-differencing scheme which does not possess this reciprocity property will have great difficulty conserving energy over long time scales.

The Curl-Differencing Function

A critical realization is that if an *E*-element is contained within a particular *B*-element's loop sum, then that *B*-element is also contained within the *E*-element's loop sign, and furthermore, the sign is the same in both loop sums! Thus, given any *E*-element and any *B*-element, let us define the curl-loop sum sign:

$$\chi_{E \times B} = 0, -1, \text{ or } +1,$$

depending on whether the elements appear in each others' loop sums, and if they do, on their sign in the loop sums. Obviously, the $\chi_{E \times B}$ is zero except whenever the *E* and *B* element are within half a cell of one another.

The Control Volume

Define a control volume, and determine the volume fraction of each field element which is interior to that volume. Call these interior fractions $[f_{vE}]$ and $[f_{vB}]$, there is a fraction number assigned to each field element.

$$0 \leq [f_{vE}] \leq 1 ,$$

$$0 \leq [f_{vB}] \leq 1 .$$

Note that they are between 0 (outside the volume) and 1 (inside the volume). In fact, most field elements will have interior fractions of exactly zero or exactly unity. Only the elements within one cell of the volume's surface will have fractional values.

Using the field update equations, we can construct the following discrete form of the Poynting theorem:

$$\begin{aligned}
& \sum_{E_elements}^{1/2} [f_{vE}] ([\mathbf{E} \cdot d\mathbf{l}]^{n+1} + [\mathbf{E} \cdot d\mathbf{l}]^n) ([\mathbf{D} \cdot d\mathbf{A}/dt]^{n+1} - [\mathbf{D} \cdot d\mathbf{A}/dt]^n) \\
& + \sum_{B_elements}^{1/2} [f_{vB}] [\mathbf{H} \cdot d\mathbf{l}]^{n+1/2} ([\mathbf{B} \cdot d\mathbf{A}/dt]^{n+3/2} - [\mathbf{B} \cdot d\mathbf{A}/dt]^{n-1/2}) \\
= & - \sum_{E_elements}^{1/2} [f_{vE}] ([\mathbf{E} \cdot d\mathbf{l}]^{n+1} + [\mathbf{E} \cdot d\mathbf{l}]^n) [\mathbf{J} \cdot d\mathbf{A}]^{n+1/2} \\
& + \sum_{E_elements}^{1/2} [f_{vE}] ([\mathbf{E} \cdot d\mathbf{l}]^{n+1} + [\mathbf{E} \cdot d\mathbf{l}]^n) \sum_{loop} [\mathbf{H} \cdot d\mathbf{l}]^{n+1/2} \\
& - \sum_{B_elements}^{1/2} [f_{vB}] [\mathbf{H} \cdot d\mathbf{l}]^{n+1/2} \sum_{loop} ([\mathbf{E} \cdot d\mathbf{l}]^{n+1} + [\mathbf{E} \cdot d\mathbf{l}]^n)
\end{aligned}$$

The first two lines are obviously the time derivatives of the standard electric and magnetic field energy, the middle line is obviously the work done on the fields by the current. The last two lines must obviously be the Poynting flux then!

Define the change in electric and magnetic energies, and the work done by the current, all having units of watts, as:

$$\begin{aligned}
[\mathbf{E} \cdot d\mathbf{D} dV/dt]^{n+1/2} & = 1/2 ([\mathbf{E} \cdot d\mathbf{l}]^{n+1} + [\mathbf{E} \cdot d\mathbf{l}]^n) ([\mathbf{D} \cdot d\mathbf{A}/dt]^{n+1} - [\mathbf{D} \cdot d\mathbf{A}/dt]^n) , \\
[\mathbf{H} \cdot d\mathbf{B} dV/dt]^{n+1/2} & = 1/2 [\mathbf{H} \cdot d\mathbf{l}]^{n+1/2} ([\mathbf{B} \cdot d\mathbf{A}/dt]^{n+3/2} - [\mathbf{B} \cdot d\mathbf{A}/dt]^{n-1/2}) , \\
[P_J dV]^{n+1/2} & = 1/2 ([\mathbf{E} \cdot d\mathbf{l}]^{n+1} + [\mathbf{E} \cdot d\mathbf{l}]^n) [\mathbf{J} \cdot d\mathbf{A}]^{n+1/2} .
\end{aligned}$$

With these definitions and the introduction of the curl loop sum sign, the Poynting theorem can be rewritten as:

$$\begin{aligned}
& \sum_{E_elements} [f_{vE}] [\mathbf{E} \cdot d\mathbf{D} dV/dt]^{n+1/2} + \sum_{B_elements} [f_{vB}] [\mathbf{H} \cdot d\mathbf{B} dV/dt]^{n+1/2} = \\
& - \sum_{E_elements} [f_{vE}] [P_J dV]^{n+1/2} \\
& - \sum_{E_elements} \sum_{B_elements} 1/2 ([f_{vB}] - [f_{vE}]) ([\mathbf{E} \cdot d\mathbf{l}]^{n+1} + [\mathbf{E} \cdot d\mathbf{l}]^n) \chi_{E \times B} [\mathbf{H} \cdot d\mathbf{l}]^{n+1/2} .
\end{aligned}$$

The last line is the Poynting flux. It is readily seen to depend on only the fields at the surface of the control volume, because on the interior, both interior fractions are unity,

and the quantity, $[f_{vB}] - [f_{vE}]$, goes to zero. Similarly on the exterior, both fractions are zero. The Poynting flux only contributes where there is a difference between $[f_{vB}]$ and $[f_{vE}]$, and this only occurs within one cell of the boundary of the control volume.

6.3 Discontinuity Operators

Define Electric and Magnetic Discontinuity Operators, \mathbf{M}_E and \mathbf{M}_B . These operators remap the fields back onto themselves, either removing components via projection, or extrapolating onto positions where the Maxwell curl equations are not well defined because of discontinuity. The operators can be written as matrices which multiply the field elements to arrive at a new set of field elements, e.g., $[\mathbf{E} \cdot d\mathbf{l}] \leftarrow [\mathbf{E} \cdot d\mathbf{l}] \cdot [\mathbf{M}_E]$. These operators provide a very general framework for applying boundary conditions, both internal and external, to Maxwell's equations. The discontinuity operators are equal to the identity operator except within one cell of a discontinuity or boundary condition. They can be introduced into Maxwell's equations as follows:

$$[\mathbf{B} \cdot d\mathbf{A}/dt]^{n+1/2} = [\mathbf{B} \cdot d\mathbf{A}/dt]^{n-1/2} - [\mathbf{M}_B^T] \cdot (\sum_{loop} [\mathbf{M}_E^T] \cdot [\mathbf{E} \cdot d\mathbf{l}]^n) , \text{ and}$$

$$[\mathbf{D} \cdot d\mathbf{A}/dt]^{n+1} = [\mathbf{D} \cdot d\mathbf{A}/dt]^n - [\mathbf{M}_E] \cdot [\mathbf{J} \cdot d\mathbf{A}]^{n+1/2} + [\mathbf{M}_E] \cdot (\sum_{loop} [\mathbf{M}_B] \cdot [\mathbf{H} \cdot d\mathbf{l}]^{n+1/2}) ,$$

where $[\mathbf{M}_E^T]$ is the transpose matrix operator of $[\mathbf{M}_E]$, and similarly for the magnetic and current operators. At first glance, the discontinuity operators appear to disrupt the Maxwell divergence equations where they are different from the identity operation; however, because these locations are within one cell of a discontinuity or boundary condition, the divergence conditions are, in fact, undefined at these locations and hence there is no actual disruption of the divergence rules.

Note that the Poynting power flux must be redefined as,

$$[\mathbf{E} \cdot d\mathbf{l}] \chi_{E \times B} [\mathbf{H} \cdot d\mathbf{l}] \rightarrow [\mathbf{E} \cdot d\mathbf{l}] \cdot [\mathbf{M}_E] \chi_{E \times B} [\mathbf{M}_B] \cdot [\mathbf{H} \cdot d\mathbf{l}] ,$$

and the work done by the current must be redefined as,

$$[\mathbf{E} \cdot d\mathbf{l}] \cdot [\mathbf{J} \cdot d\mathbf{A}] \rightarrow [\mathbf{E} \cdot d\mathbf{l}] \cdot [\mathbf{M}_E] \cdot [\mathbf{J} \cdot d\mathbf{A}] ,$$

and the electric field used for particle forces must similarly be replaced by $[\mathbf{E} \cdot d\mathbf{l}] \cdot [\mathbf{M}_E]$. The electric and magnetic energies remain unaffected, though. This latter fact highlights an important property of the discontinuity operators. They do not alter the definition of stored energy in the electromagnetic fields, they only affect the way power is transferred between fields within the cell containing the discontinuity.

6.4. Roadmap

The slides from the MAGIC Users Group Talk follow. Note slides 4 & 5, which include simulations performed in this project.



Roadmap for Eliminating Stair-Stepping and Grid-Snapping

David N. Smith
Mission Research Corporation

Prepared for:
MAGIC Users Group Meeting
Monterey, California
June 22, 1999

Sponsored by:
Air Force Office Of Scientific Research

MRC/WDC-B-468-01



Overview

- What is Stair-Stepping and Grid-Snapping
 - And why, after all these years, do we want to get rid of them?
- State of the Art (in MAGIC)
 - SHIM and QUARTERROUND
- Future Roadmap for Fields
 - Better Partial Cells
- Future Roadmap for Particles
 - Introduce Image Particles

MRC/WDC-B-468-2



What's the Problem?

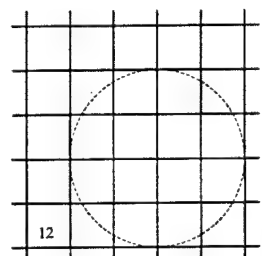
Circle: Diameter = 4 cells, Volume = $12\frac{1}{2}$ cells

3-D

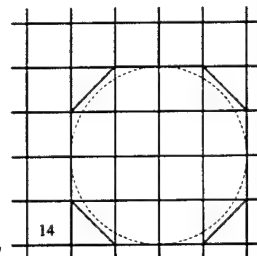
2-D

- Stair-Stepping:

- Metal conductors are solid blocks, or half-blocks, instead of curved surfaces.
- Problem: Wrong volume.



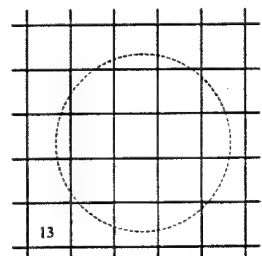
Marked



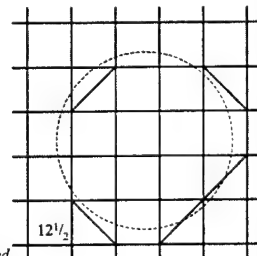
Marked

- Grid-Snapping:

- Average surface location is displaced to nearest grid coordinate.
- Problem: Distorted shape.



Unmarked



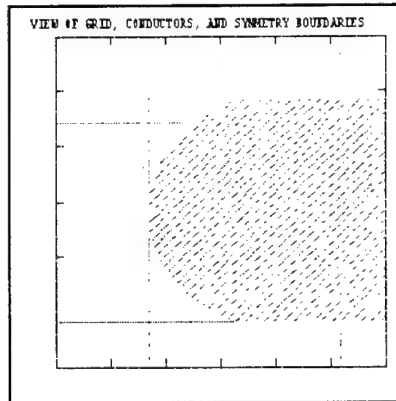
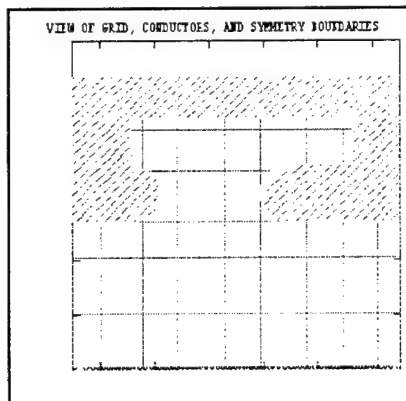
Unmarked

MRC/WDC-B-468-3



Anti-Stair-Stepping State-of-the-Art

- In 2-D, use QUARTERROUND area, MARK, to match diagonals to curved surface, *and get good field profile*.



(Courtesy of Daryl Sprehn, SLAC)

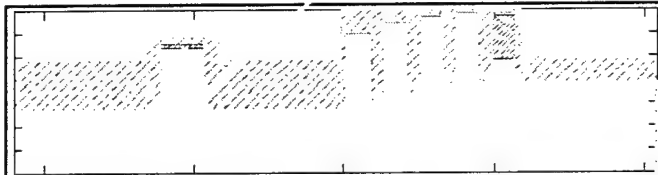
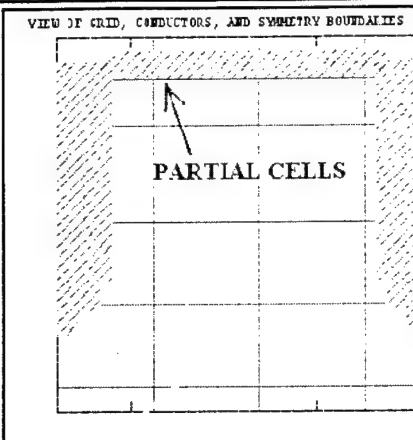
- In 3-D, no diagonals, so stair-stepping is always present.

MRC/WDC-B-468-4



Anti-Grid-Snapping State-of-the-Art

- In 2-D, use SHIM, for a “partial cell”, *to give proper radius and proper cavity frequency.*
- In 3-D, no SHIM, so grid-snapping is always present.



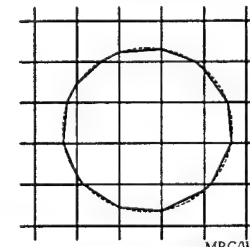
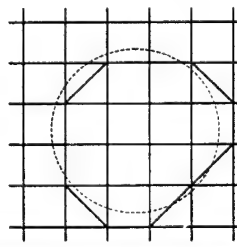
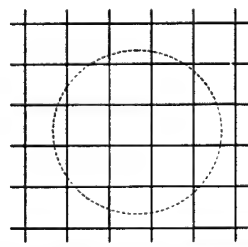
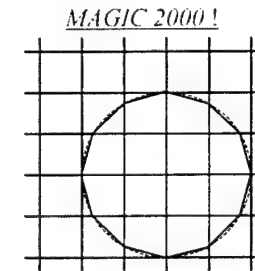
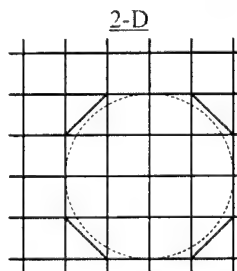
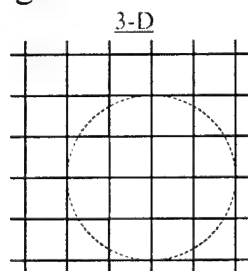
(Courtesy of Liqun Song, SLAC)

MRC/WDC-B-468-5



Partial Cell Solution

- Generalize SHIM for arbitrary “partial cell”, based on grid-line intersections.



MRC/WDC-B-468-6



Roadmap for Fields

- New Geometry Engine
 - Back to surface modeling !
 - Automatic SHIM'ing.
 - Stand-alone version nearly complete, code integration is next step.
- Firm Mathematical Foundation
 - “Extrinsic Elements” formulation (insures no energy leaks)
 - Area Re-mapping (defeats Courant difficulties)

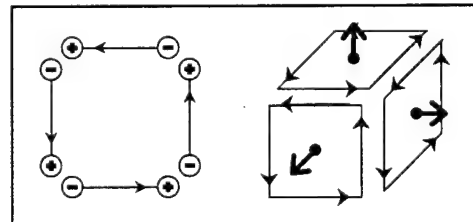
MRC/WDC-B-468- 7



“Extrinsic Elements”

- Basically, it's a certain normalization of Finite-Integrals.
- Separate E, H, D, B elements have “extrinsic” units, e.g., volts, not volts/meter.

- » $[E \cdot dI]^n$ (volts)
- » $[D \cdot dA/dt]^n$ (amps)
- » $[H \cdot dI]^{n+1/2}$ (amps)
- » $[B \cdot dA/dt]^{n+1/2}$ (volts)
- » $[J \cdot dA]^{n+1/2}$ (amps)
- » $[\rho dV/dt]^n$ (amps)



- All derivatives, $\nabla, \nabla \cdot, \nabla \times, \partial_t$, become matrices of 0, ±1's.
- Partial cells trivial, because of integral element definition.

MRC/WDC-B-468- 8



Maxwell with Extrinsic Elements

- Equations are:

$$\begin{aligned} \gg [\mathbf{B} \cdot d\mathbf{A}/dt]^{n+1/2} &= [\mathbf{B} \cdot d\mathbf{A}/dt]^{n-1/2} - \sum_{loop} [\mathbf{E} \cdot d\mathbf{l}]^n \\ \gg [\mathbf{D} \cdot d\mathbf{A}/dt]^{n+1} &= [\mathbf{D} \cdot d\mathbf{A}/dt]^n + \sum_{loop} [\mathbf{H} \cdot d\mathbf{l}]^{n+1/2} - [\mathbf{J} \cdot d\mathbf{A}]^{n+1/2} \\ \gg \sum_{star} [\mathbf{B} \cdot d\mathbf{A}/dt]^{-1/2} &= 0 \\ \gg \sum_{star} [\mathbf{D} \cdot d\mathbf{A}/dt]^0 &= [\rho dV/dt]^0 \\ \gg \sum_{star} [\mathbf{J} \cdot d\mathbf{A}]^{n+1/2} &= [\rho dV/dt]^n - [\rho dV/dt]^{n+1} \end{aligned}$$

- All detail (and approximation) is in constitutive relations:

$$\begin{aligned} \gg [\mathbf{H} \cdot d\mathbf{l}]^{n+1/2} &= [dl dt / \mu dA] [\mathbf{B} \cdot d\mathbf{A}/dt]^{n+1/2} \\ \gg [\mathbf{E} \cdot d\mathbf{l}]^n &= [dl dt / \epsilon dA] [\mathbf{D} \cdot d\mathbf{A}/dt]^n \end{aligned}$$

- All non-uniform grid and material factors lumped together !

$$\begin{aligned} \gg [dl dt / \mu dA], &\text{ one per } \mathbf{E} \text{ element} \\ \gg [dl dt / \epsilon dA], &\text{ one per } \mathbf{B} \text{ element} \end{aligned}$$

MRC/WDC-B-468- 9



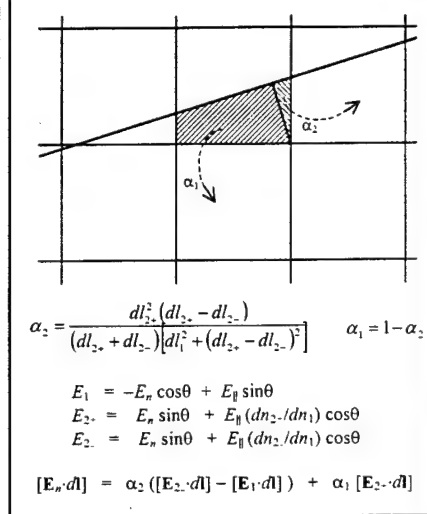
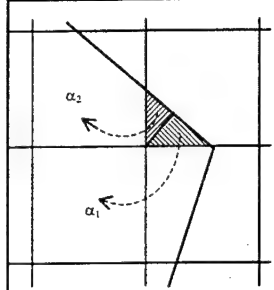
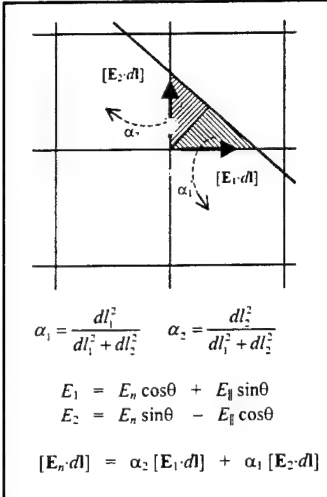
Courant and Energy

- Partial cells use the **non-metallic** dl and dA in the constitutive factors.
 - Problem: $dl/dA \rightarrow \infty$ for small triangles \Rightarrow Destroys Courant !
 - Solution: Remove **B**-element, re-map triangle area to neighbors.
 - Rule: Any partial cell with less than half area *must* be re-mapped.
- Symmetry of Maxwell is necessary to prevent energy leaks.
 - Problem: Removing **B**-element destroys symmetry of Maxwell.
 - Solution: Re-map $\nabla \times \mathbf{E}$ to neighbors in same fashion as area.
 - Rule: Transpose re-map operator for $\nabla \times \mathbf{E}$ *must* be used to extrapolate back **H**.

$$\begin{aligned} \gg [\mathbf{B} \cdot d\mathbf{A}/dt]^{n+1/2} &= [\mathbf{B} \cdot d\mathbf{A}/dt]^{n-1/2} - [\mathbf{M}_B] \cdot \sum_{loop} [\mathbf{E} \cdot d\mathbf{l}]^n \\ \gg [\mathbf{D} \cdot d\mathbf{A}/dt]^{n+1} &= [\mathbf{D} \cdot d\mathbf{A}/dt]^n + \sum_{loop} [\mathbf{M}_B'] \cdot [\mathbf{H} \cdot d\mathbf{l}]^{n+1/2} - [\mathbf{J} \cdot d\mathbf{A}]^{n+1/2} \end{aligned}$$

MRC/WDC-B-468- 10

Re-mapping Coefficients

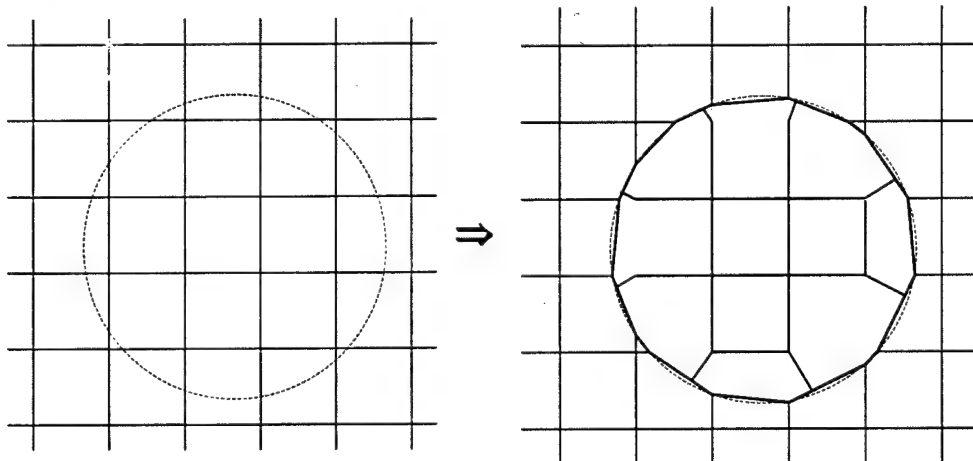


- If coefficients equal area fractions \Rightarrow cancels E_{\parallel} .
- $[E \cdot dI]$ elements appear only in the combination $[E_n \cdot dI]$.

(Present SHIM: $\alpha_1=1$, $\alpha_2=0$,
good for gentle slope only.)

MRC/WDC-B-468- 11

“Effective” Result of Re-mapping



But no strange shapes in code, it's really same old rectangles with re-maps:

$$[\mathbf{B} \cdot d\mathbf{A}/dt]^{n+1/2} = [\mathbf{B} \cdot d\mathbf{A}/dt]^{n-1/2} - [\mathbf{M}_B] \cdot \sum_{loop} [\mathbf{E} \cdot dI]^n$$

$$[\mathbf{D} \cdot d\mathbf{A}/dt]^{n+1} = [\mathbf{D} \cdot d\mathbf{A}/dt]^n + \sum_{loop} [\mathbf{M}_B'] \cdot [\mathbf{H} \cdot dI]^{n+1/2} - [\mathbf{J} \cdot d\mathbf{A}]^{n+1/2}$$

MRC/WDC-B-468- 12



Roadmap for Particles

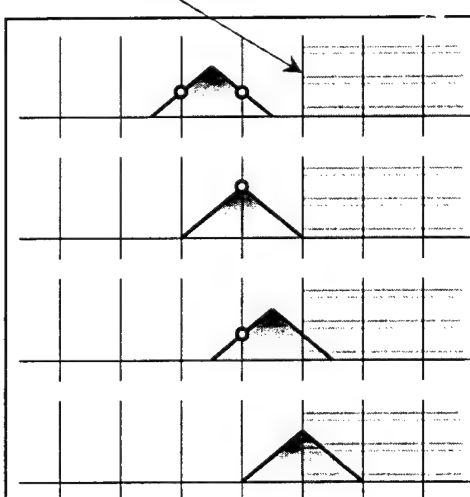
- Kill events are a problem with partial cells, because particle still has charge on interior grid points at moment of destruction. Similar for creation events.
- Boundary “image particles” can resolve problem.
- Image charge computation, and source code, is intensive !

MRC/WDC-B-468- 13

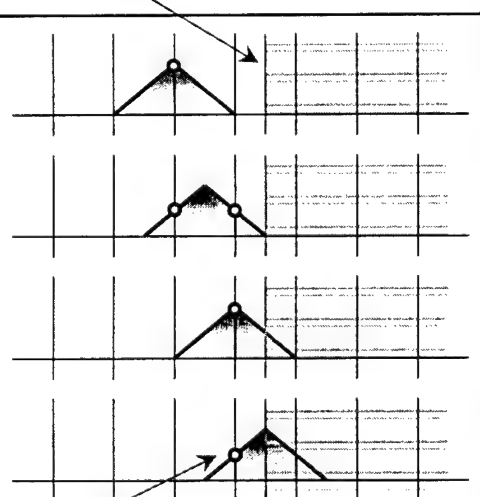


The Particle Kill Problem

Full Cell Boundary



Partial Cell Boundary



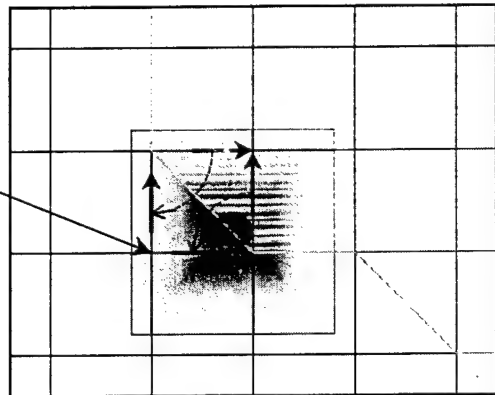
Interior Charge at Moment of Destruction

MRC/WDC-B-468- 14



State-of-the-Art

- In 2-D, particles can be killed on diagonal surfaces, leaving charge at one interior grid point.
- For a perfect one-to-one diagonal, the accumulated currents inside the metal triangle are the mirror of the image charges.
- So fast *per-cell* images, rather than *per-particle*, but only for perfect diagonals.

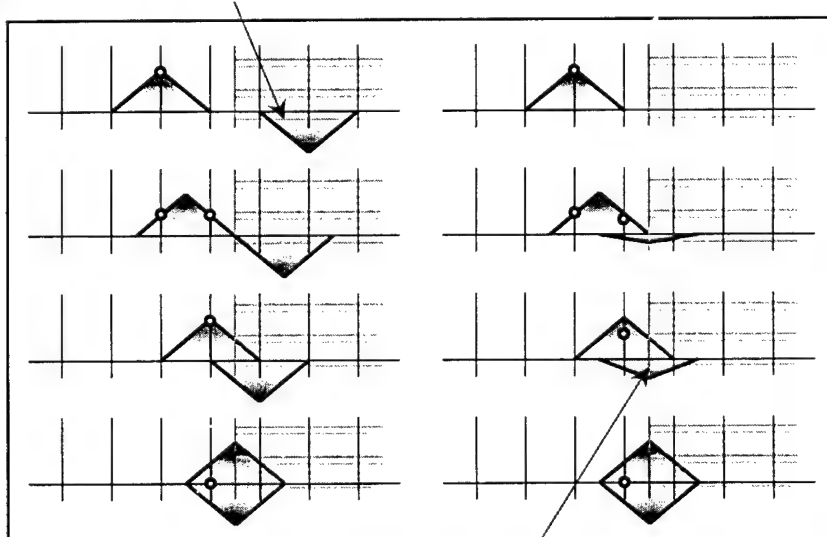


MRC/WDC-B-468- 15



Image Charges in 1-D

Type I: Opposite Charge Mirrors Kinematics



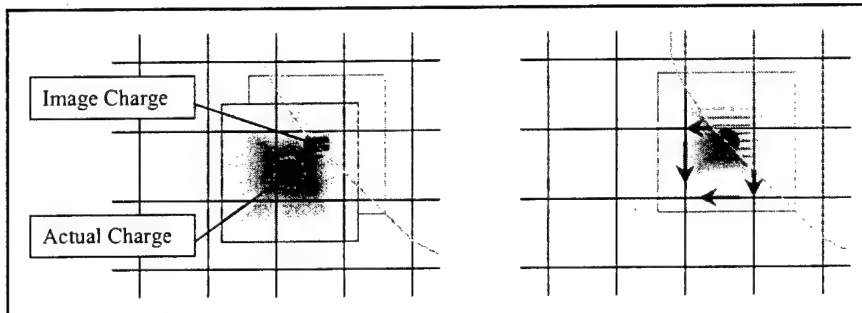
Type II: Fixed Image Grows Opposite Charge

MRC/WDC-B-468- 16



Image Charges in 2-D and 3-D

- Mirrored Kinematics is difficult on curves and in corners. Instead the Fixed Image method will be probably be used.
- Fixed images require a path from the metal to each of the interior grid locations. There is always a path, but coding this aspect will be challenging.



MRC/WDC-B-468- 17



Summary

- Faster better computers mean bigger, more realistic simulations, with more components. This means more time spent on understanding and resolving gridding conflicts.
- A comprehensive roadmap is in place to eliminate the primary cause for grid conflicts, e.g., stair-stepping, and grid-snapping.
- First bring the partial-cell methodology of SHIM to its full potential. Second introduce image methods for particle kill and creation.

MRC/WDC-B-468- 18

7. High Perveance Klystron Issues

Author's Note - This section is based upon a talk given at the NRL vacuum electronics weekly seminar on January 12, 1999. The title of the talk was "Simulations of Multiple Beam, Sheet, and Triaxial Klystrons." At the time of the talk, this author was struck by the commonality of purpose inherent in these three different approaches to obtaining higher power by means of defeating the conventional 1-2 micropervs limit on beam current. All three methods were also undergoing investigation by the author, under three differently funded projects. Only part of the talk focused on the GMBK, nevertheless, the entire talk is presented here for completeness. Also, this constitutes the only place that this talk has been written up in report form.

7.1 The High Frequency Scaling Problem

The desire for high perveance beam klystrons is directly related to the issue of higher power at higher frequency. The cross-section size of the beam must scale with the wavelength, λ , if one is to fit the beam inside of a cavity, which must necessarily be roughly $\frac{1}{2}$ a wavelength in size. If one assumes the inevitable upper limit on the cathode emission density state-of-the-art, say 10-20 amps/cm², then beam current scales as cross-section area: Current $\sim \lambda^2$. If one also assumes that, for practical reasons, the klystron will be built at as low a voltage as possible, then the conventional pencil beam perveance is around 1 micropervs, and so: Voltage $\sim I^{2/3} \sim \lambda^{4/3}$. This means that:

$$\text{Power} \sim \lambda^{10/3} \sim (1/\text{frequency})^{10/3}.$$

In other words, for fixed state-of-the-art cathode technology, and low voltage operation, power will scale inversely with frequency to the 3.3 power, e.g., a factor of 10 increase in frequency is accompanied by a factor of 1000 decrease in power. There are only three ways to remove oneself from this restrictive power limitation curve:

- a) improve cathode emission densities,
- b) defeat the 1 microperv limitation, or
- c) operate at higher voltage.

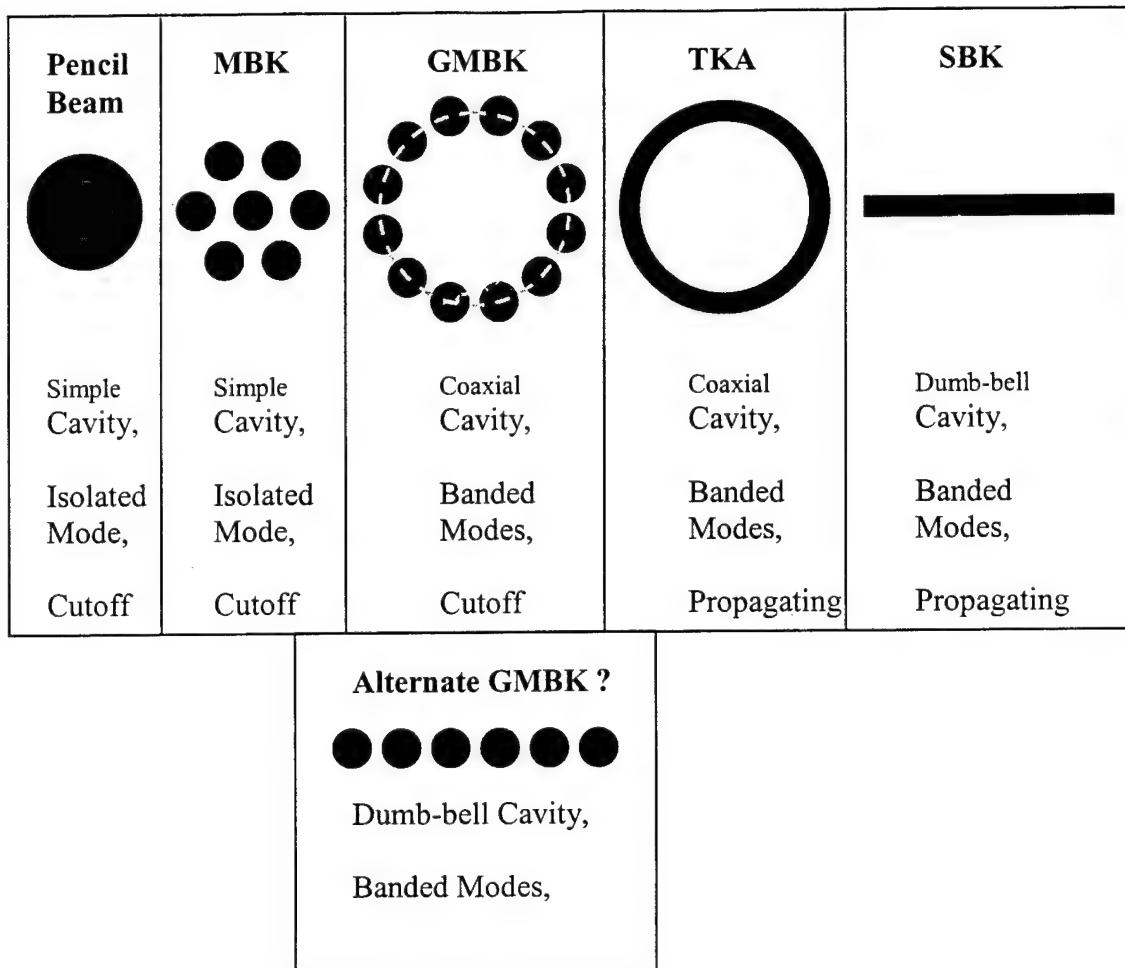
The focus of this talk is the second method, of course; other DoD programs are actively researching the first and third alternative. The third alternative involves more than just a question of high voltage operation when the voltage becomes relativistic, and again, other DoD programs have researched the relativistic klystron alternative. The applications for higher power at higher frequency are quite diverse, and include RF sources for the Next Linear Collider and for civilian and military radar. However, additional DoD interest in the second method is generated by the fact that defeating the space charge limitation around 1 microperv is possibly accompanied by an inherent increase in radar bandwidth. The hot-test bandwidth of a cavity contains a term in beam perveance, which can dominate over the conventional cavity Q for high perveances, thus potentially allowing the second method to get two simultaneous benefits, e.g., higher power at high frequency and wider bandwidth.

7.2. The High Perveance Klystron Gallery

The space-charge limitation around 1 microperv is defeated by rearranging the geometry of the drift tube in such a way that, for any point in the beam cross-section, there is metal drift tube closer to the point than most of the remaining beam space charge. Many ways of accomplishing this have been suggested, the figure below illustrates some of the methods that have been simulated in 3-D by MRC. Interestingly, they can be arranged in a peculiar fashion with various stages of progression, from the traditional pencil beam at one extreme, to the Sheet Beam Klystron (SBK) at the other extreme.

The hexagonal-packed Multiple Beam Klystron (MBK) is the first stage in progression away from the conventional pencil beam. It simply divides the beam into cylindrical beamlets, each in its own drift tube, but with all drift tubes opening up into the same traditional shaped reentrant-cavity. This works well, so long as the total size of the beam cross-section doesn't exceed about $\frac{1}{4}$ -wavelength, at which point there is significant gap-voltage difference between inner and outer beamlets at the cavity.

The next step of the progression, which is the geometry of the Gigawatt Multiple Beam Klystron (GMBK), is to rearrange the beamlets into a circular pattern, and use a coaxial cavity. The total length around the cavity can be considerably greater than $\frac{1}{4}$ -wavelength, and there is, in principle, no limit to how many beamlets one can use. There is a price to pay for going this next step in the progression, though; the coaxial cavity has a banded-mode-structure, with easily excitable modes close to operating mode in frequency. This could potentially result in phase differences between the beamlets. (On the other hand, one could imagine purposely running at one of the higher modes in the band, where frequency separation is greatest, and then simply omitting the beamlets which would occur at the nodes of the higher mode. I'm not sure if such an idea has ever been seriously looked at, though.)



Gallery of different types of High Perveance Klystron configurations.

The next step of the progression is to sew the circular arrangement of beamlets back together, so that now the beam appears as a hollow cylindrical shell, with drift-tube both inside and outside the beam. The combination of inner drift-wall, beam, and outer drift-wall is a “triaxial” arrangement, hence the name, Triaxial Klystron Amplifier (TKA). The inner metal conductor is what distinguishes this geometry from a traditional klystron with a hollow beam. In addition, the inner metal conductor is believed to greatly reduce the traditional diocotron-instability concerns of the hollow beam. Note that this effectively uses the same coaxial cavity as the GMBK geometry. The price to be paid for this step is that the drift tube is now a coax, and a coax is no longer cut-off at the operating frequency. Hence, the concern for undesirable feedback and oscillation between the cavities is considerable in this geometry. (There is also concern in supporting and grounding the inner coax, however, this seems to have successfully managed in the TKA program.) The primary gain from taking this step is that high-current hollow-beam cathode technology is considerably simpler than multiple-beam cathode technology.

The final step in the progression is to slice the hollow beam, and straighten it out into a flat sheet, resulting in the Sheet Beam Klystron (SBK), which perhaps could be considered to be the epitome of high-perveance geometry. It is also arguably the most difficult, since it requires an unfamiliar cavity shape, such as the “dumb-bell” cavity proposed by SLAC, which has banded-mode properties similar to the coaxial cavity. It also requires novel beam generation and focusing methods, which have only recently been demonstrated. Nevertheless, the SBK is much more compact than the TKA, in one of the directions, and has a geometry which is practical for micro-machining, e.g., making it the obvious choice for the highest frequencies.

Finally, it should be noted that one other obvious geometry is possible, namely an alternate linear arrangement of beamlets in the GMBK, instead of the coaxial arrangement, see the illustration. This would be equivalent to the GMBK except for substitution of the SBK dumb-bell cavity in place of the coaxial cavity. To the best of my knowledge, this arrangement has never been investigated. However, it might offer some advantage in terms of compactness and cutoff drift tubes, or perhaps it might function as a more easily realizable test-vehicle for study of the SBK cavity properties.

More detail of each of the various high perveance beam options can be found in the following sources:

MBK

“3-D Simulations of Multiple Beam Klystrons,” by David N. Smithe, Mike Bettenhausen, Larry Ludeking, G. Caryotakis, Daryl Sprehn, and Glenn Scheitrum, published in AIP Proceedings 474, of the RF 98 Workshop, Pajaro Dunes, CA, October 1998.

GMBK

“Gigawatt Multibeam Klystron (GMBK),” by G. Caryotakis, E. Jongewaard, R. Phillips, G. Scheitrum, and S. Tantawi, presented at 11th International Conference on High Power Particle Beams, Prague, Czech Republic, June 1996. Also see: <http://www.slac.stanford.edu/grp/kly/muri/murid.htm>.

TKA

“Elimination of Pulse Shortening in High-Power Microwave Tubes,” by John Pasour, David Smithe, Moshe Friedman, and Robert Richter-Sand, AFRL-DE-PS-TR-1998-1033, April 1988.

“Modulating electron beams for an X band relativistic klystron amplifier,” by M. Friedman, J. Pasour, and D. Smithe, Applied Physics Letters 71 (1997), pg. 3724.

SBK

“W-Band Sheet Beam Klystron Simulation,” by E. R. Colby, G. Caryotakis, W. R. Fowkes, and D. N. Smithe , published in AIP Proceedings 474, of the RF 98 Workshop, Pajaro Dunes, CA, October 1998.

7.3. Frequency Scaling for High Perveance Solutions

It was seen that the power-frequency scaling of the traditional klystron, under the assumption of minimum voltage and fixed cathode technology, goes like $\text{frequency}^{-10/3}$. What is the expected scaling of the various high-perveance beam devices? Simplistically, one would expect the MBK to simply multiply the existing scaling by N , the number of beamlets, e.g.,

$$\text{Power}_{\text{MBK}} \sim \lambda^{10/3} N,$$

which is the product of current and voltage according to: $\text{Power} \sim \text{Current} \times \text{Voltage} \sim (\lambda^2 J N) \times (\lambda^2 J)^{2/3} \sim (I) \times (I/N)^{2/3}$, where voltage is constrained by the approximate 1 microperv relation on the single beamlet current, I/N . Observe that this contains the implication that if we divide the same current into more beamlets, the minimum voltage can be made to drop, but at a cost in reduced power. In fact, dividing up the beam into smaller beamlets is indeed a possible means of achieving lower voltage operation, if one is willing to accept the loss in power. However, in this case we are interested in adding more beamlets at fixed voltage in order to get more power. So while the MBK still has the unfortunate $\text{frequency}^{-10/3}$ power scaling, it can be offset with the N scaling on the number of beamlets.

But there are additional constraints for MBK scaling. Recall that the hexagonal-packed MBK uses a traditional cavity, whose size is constrained by the wavelength, in all directions. The total ensemble of the beam cross-sectional area cannot exceed the size of the cavity. In addition, wall thickness issues and machining difficulties at the small size of the higher frequencies also constrain the number of beamlets in such an MBK. Thus, the scaling above has a definite and ultimate upper limit on N . This makes it rather difficult to use the scaling formula to estimate Power vs. Number of Beamlets. Hence the emphasis on 3-D modeling tools.

The scaling in the case of the TKA and the Sheet Beam Klystron (SBK) is somewhat more practical. Here the current scaling is $\text{Current} \sim \lambda J L$, where L is the rather arbitrary perimeter of the TKA beam, or length of the sheet beam. The perveance of these beams is based upon the current-per-unit-length, e.g., $\text{Voltage} \sim (\lambda J)^{2/3}$, since in principle, the cathode can be extended ad-infinitum. So the TKA and SBK power scaling goes like:

$$\text{Power}_{\text{SBK}} \sim \lambda^{5/3} L,$$

The $\lambda^{5/3}$ scaling is much more favorable for high power at high frequencies, and the L scaling is much more reliable and does not have the firm upper limit the the MBK has.

Where does the GMBK fit in? Unlike the MBK, the number of beams is not restricted. One would tend to think that the GMBK should have similar scaling properties as the TKA, the former simply being a division of the TKA's annular beam into beamlets arranged in the same annulus, both using similar cavity shapes. If one

takes the product of (λN) in the GMBK as representing the length, L , in the SBK, then the MBK power scaling turns into $\lambda^{7/3}L$ instead of $\lambda^{5/3}L$. The additional factor of $\lambda^{2/3}$ is due to the type of cathode, either individual beamlets, or combined sheet.

There is, in fact, a general argument for a scaling that is in-between the beamlet and sheet-beam scalings, and would apply to all high perveance scenarios, in general. If one simply states that the voltage of any high perveance diode depends on J only, e.g., as it does for an infinite planar diode, then the MBK, GMBK, TKA, and SBK are all equivalent, and become:

$$\text{Power} \sim \lambda^2 L \sim \lambda^3 N,$$

This universal scaling is easier to remember, and given the great variations of diode geometry, may not be any less accurate.

7.4. Design Parameters to Date

The approximate target parameter ranges for each of these devices was:

MBK

3 GHz, 1 Megawatt, 12% bandwidth

GMBK (Annular MBK)

1.5 GHz, 2 Gigawatt, 1 microsecond pulse

TKA

10 GHz, 1 Gigawatt, 1 microsecond pulse

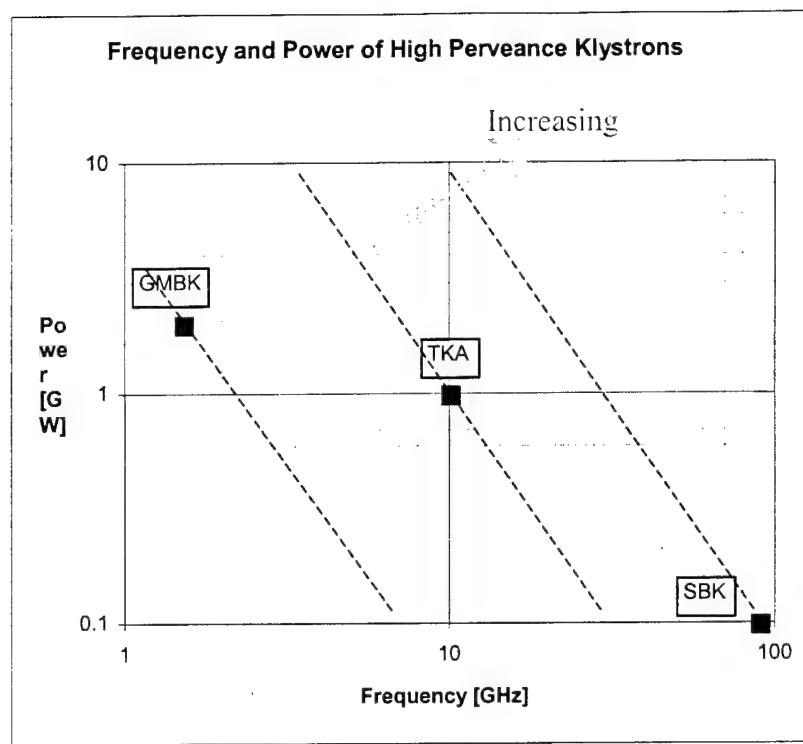
SBK

90 GHz, 100's of Megawatts, 10-20 nanosecond pulse, or 10 Megawatts, 50-100 nanosecond pulse

In particular, the 19-beam MBK at 3 GHz was to be of a wider band than is typical of the klystron, and the larger beam loading of the MBK was thought to assist in achieving this goal.

An illustration of power-frequency parameters of the three pulsed devices is shown below, together with a dotted line expressing a $\text{power} \sim \text{frequency}^{-2}$ relationship. Note that if all device shapes were equivalent, one would expect all three to lie on the same dotted line. The fact that they do not lie on the same line indicates that there are inherent advantages for one shape of high perveance beam over another. In fact, the obvious conclusion is that for maximum power at high frequency, the Sheet Beam Klystron line is the optimum. Of course, the SBK is also the most difficult to realize in practice, and one must recall that, except for some experimental results from the TKA, this chart is of "target" parameters, not achieved parameters. It is also tempting to speculate that the more to the left the line is, the more likely it is that the device can be

achieved in short order – hence, the original GMBK is probably quite realizable, in comparison to the other more technically challenging high permeance devices.



Frequency and Power comparison of MRC's high perveance klystron projects. The GMBK appears most realizable, the SBK appears to be the most technically challenging.

The following table lists the experimental state-of-the-art (in 1998) for the various high perveance devices.

MBK

Well established in Russian tube industry at medium power range (100's kW, 10% bandwidth). Also some devices built in France. Simulation of high power concepts in USA.

TKA

Beam and buncher demonstrated at NRL. Output structure under design. Similar geometry RKA verified frequency scaling as approximately f^2 .

SBK

Beam transport problems addressed successfully. Some limited cold test of components. Simulation effort just underway.

Given the above figure, indicating the widely disparate power-frequency lines of the GMBK, TKA, and SBK, it is tempting to ask what is the origin of these differences, e.g., why didn't they line up on the same line? Two issues contribute here. First is the

fact that with these high perveance beam designs, the pertinent parameter is not so much power, as power per beamlet, or power per unit beam width. Thus one can scale up the power, at the same frequency, simply by changing the number of beamlets, or the width of the sheet beam. E.g., the high perveance design offers a free parameter, for increasing power, with most other parameters fixed. Second is the fact that each different type of high perveance cross-section implies a different type of cavity, and the cavity parameters have an, here-to-fore, unmentioned impact as well.

Consider the penultimate cavity. This cavity does not extract power, but has the highest gap voltage, which is on the order of the beam voltage, and sees an RF current which is an appreciable fraction of the current. In the traditional klystron analysis, also useful for the MBK, the parameter quantifying the cavity stored energy is the shunt resistance-to-Q ratio (R/Q), and the parameter quantifying the gain-bandwidth tradeoff is Q , and the maximum gap voltage, at center-band, relates to the RF beam current according to:

$$V \sim Q(R/Q)I.$$

Consider a graph with current, I , on one axis and voltage, V , on the other axis. One can draw one line representing the diode, $V \sim I^{2/3}$, which the klystron will only operate above, and another line, $V \sim Q(R/Q)I$, representing the cavity, which the klystron will only operate below. A figure of this situation is shown below. The product of IV is, of course, the power. Notice how the Q of the cavity changes the slope of the cavity line, with a lower Q (lower gain/higher bandwidth) forcing a higher power operating point for the same cavity.

Now consider the same situation for the TKA or Sheet Beam cases, where there is the additional flexibility of the beam width parameter, L . The stored-energy of a cavity is

$$U = \frac{1}{2} \frac{V^2}{\omega(R/Q)} ,$$

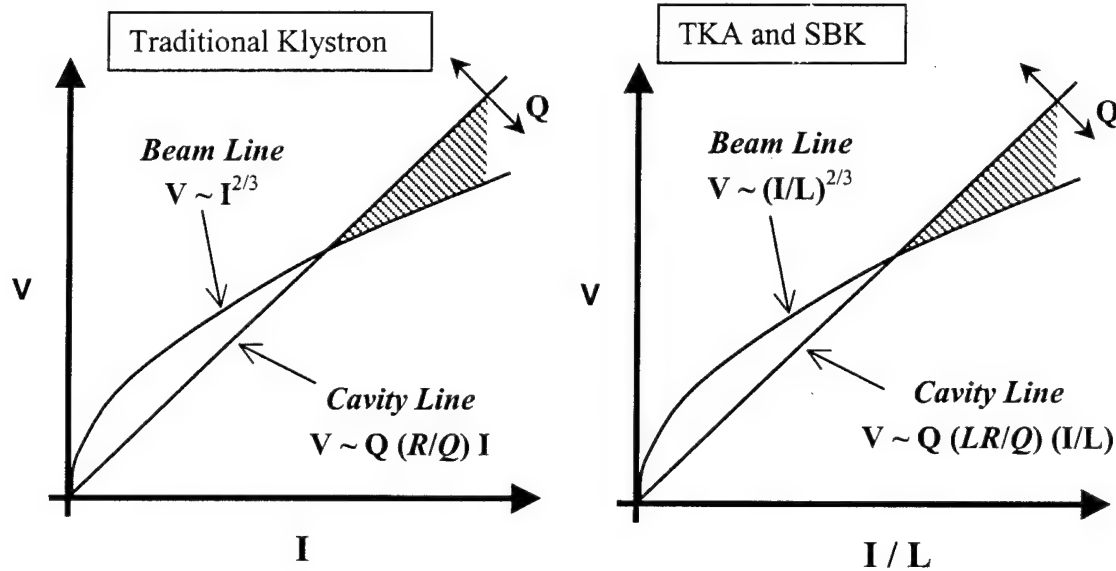
so the stored-energy-per-unit-length is

$$U/L = \frac{1}{2} \frac{V^2}{\omega(LR/Q)} ,$$

where not (LR/Q) is the stored energy parameter. In fact, it has been observed that the sheet beam klystron cavities have very low (R/Q) parameters, below anything one is accustomed to from traditional klystron design work. However, this should not come as any surprise. Extending the cavity for a wider beam simply lowers (R/Q) . Thus, it is likely that in the future, SBK design work will concentrate on the quantity (LR/Q) , e.g., the cavity's ohm-meters, rather than (R/Q) , because the former is much less sensitive to the beam width parameter, L . Similarly, the fixed perveance beam line goes as $(I/L)^{2/3}$, rather than $I^{2/3}$, and the cavity line becomes

$$V \sim Q (LR/Q) (I/L)$$

Thus, the conversion from traditional klystron design formulae to SBK design formula is a simple matter of replacing I with I/L , and (R/Q) with (LR/Q) . In the traditional picture, the product of the axis is IV , e.g., power. In the SBK picture, it is $(I/L)V$, e.g., power-per-unit-length.

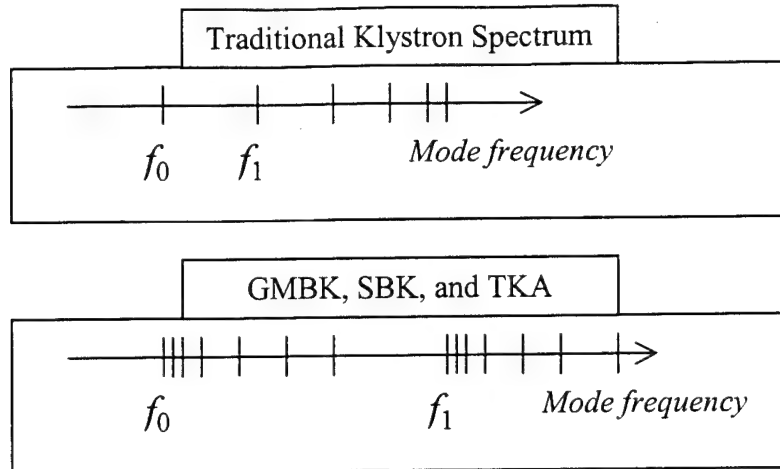


Analytic design for the case of the TKA and SBK. Properly rescaling the current, R/Q , and the power by the sheet beam length allows simpler design, with the sheet length as a free parameter.

7.5. Cavity Issues

Now consider more closely the case of the TKA, SBK, and GMBK, which do not have the firm upper limit on the length parameter, such as the MBK has on the number of beams. Is sheet beam width truly a free parameter with no limit? Surely there must be some trade-off involved ... let us pursue this question.

Obviously, a wider beam may create more difficulties in the diode region, and may be subject to additional beam focusing issues. However, there is one issue involving a direct tradeoff with beam width. This involves the banded structure of the coaxial and dumb-bell shaped cavities. In a traditional klystron cavity, the operating mode is typically the lowest mode of the cavity, and is isolated from other similarly polarized modes. This is illustrated in the figure below, where f_0 ($N_\phi=0$, $N_r=1$, $N_z=0$) is the operating mode, and f_1 is the next mode up, with mode number of either $N_\phi=1$, $N_z=1$ or an $N_r=2$. The frequency spectrum for a Sheet Beam Klystron (also TKA and GMBK) is different by virtue of the fact that the modes with non-zero mode-number along the width of the beam can be very closely spaced, leading to a banded spectrum, as illustrated in the lower part of the following figure. In that case, f_1 still designates the next radial or axial mode, but the beam-width mode numbers cluster closely to the operating mode.



Difference in the mode structure of a traditional klystron (and MBK), compared to the GMBK, SBK, and TKA.

The mode spacing near the operating frequency is given fairly accurately by:

$$\frac{\delta f}{f_0} = \frac{1}{8} \frac{n^2 c^2}{f_0^2 L^2}, \text{ for } n = 0, 1, 2, 3, \dots,$$

where L is the sheet beam width (or $\frac{1}{2}$ the TKA or GMBK beam perimeter). If one desires the nearest mode to be out-of-band, e.g., outside $\delta f/f_0 = (2Q)^{-1}$, then this requires cavity Q's exceeding the following relation,

$$Q > \left(\frac{2Lf_0}{c} \right)^2.$$

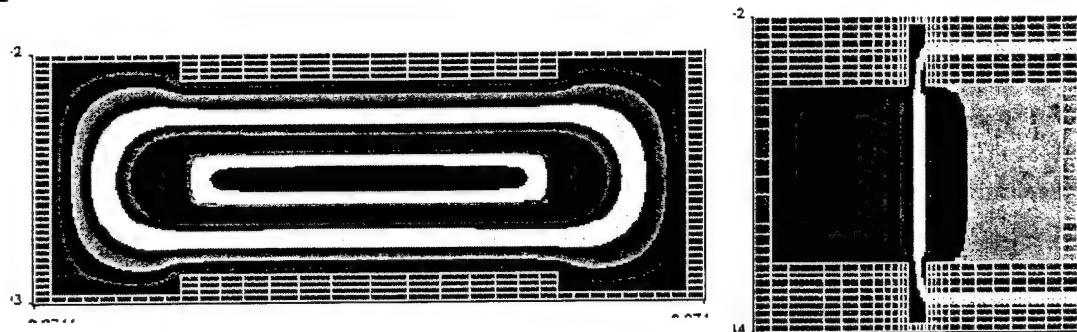
Since the coaxial or dumbbell cavity is likely to be $\frac{1}{2}$ a wavelength in height, this implies that the Q must exceed the square of the ratio of cavity width-to-height. From a cold-test point of view, this is not likely to be a problem for initial sheet beam geometry, where the cavity width will likely be at most 10 times the height, and Q's need to be comfortably above 100 anyway. However, recall that the beam loading can alter frequency and bandwidth, and this effect is magnified in high perveance situations. Thus, a safe conclusion for hot-test is not trivial. If there were to be difficulties, one would observe that different parts of the beam would not stay in phase with each other, as competing $N_{width} \neq 0$ modes amplified.

Simulations of a 3-cavity W-band SBK (see previous reference) have, in fact, been made by Eric Colby of SLAC to test this issue, as well as other issues. Happily, these simulations have shown good phase coherency across the beam. Nevertheless, this discussion shows that the sheet beam cannot be extended ad-infinitum, without suffering a transition to a more dangerous situation where competing modes are in-band. The dependence on the square of the width-to-height ratio also implies that one might

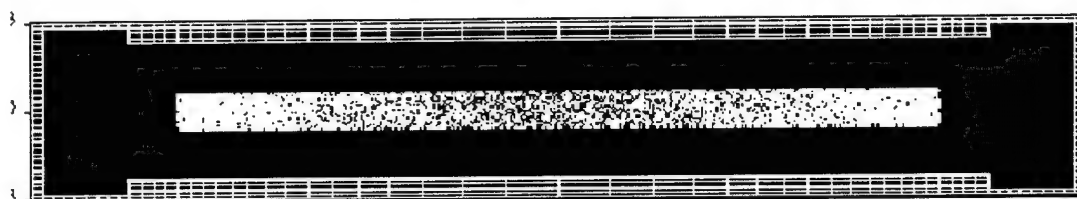
encounter this transition rapidly, if SBK technology advances to the point where the cavity is about about 30 times wider than it is high.

The figures below show a) the cold-test field patterns from simulations with an integrated potential view across the width of the beam, b) a cross-section view of electrons in a dumbbell-type cavity, and c) a view of the bunching in the 3-cavity hot test.

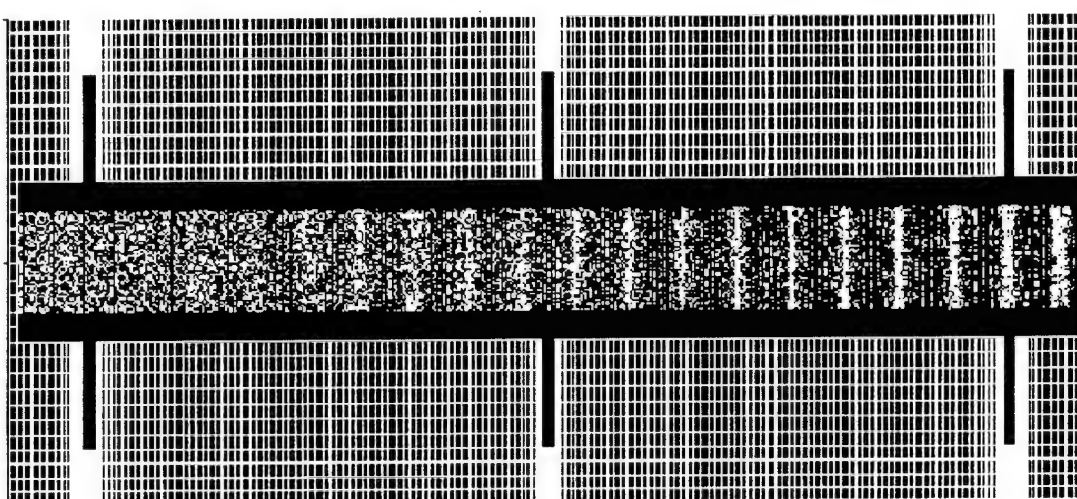
a)



b)



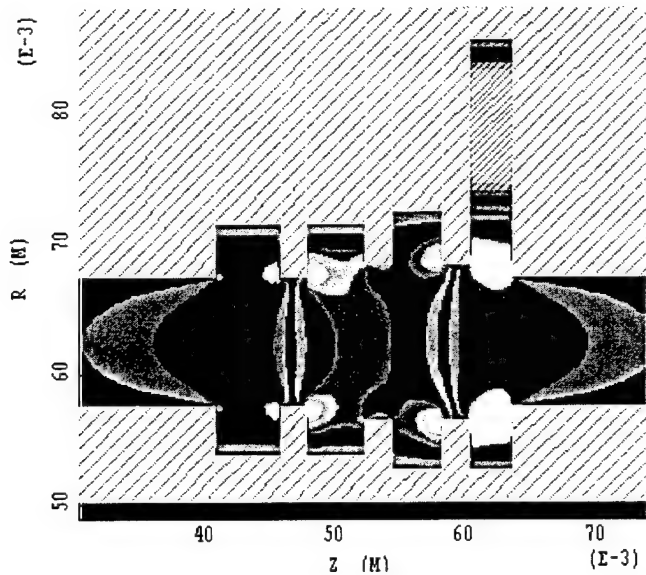
c)



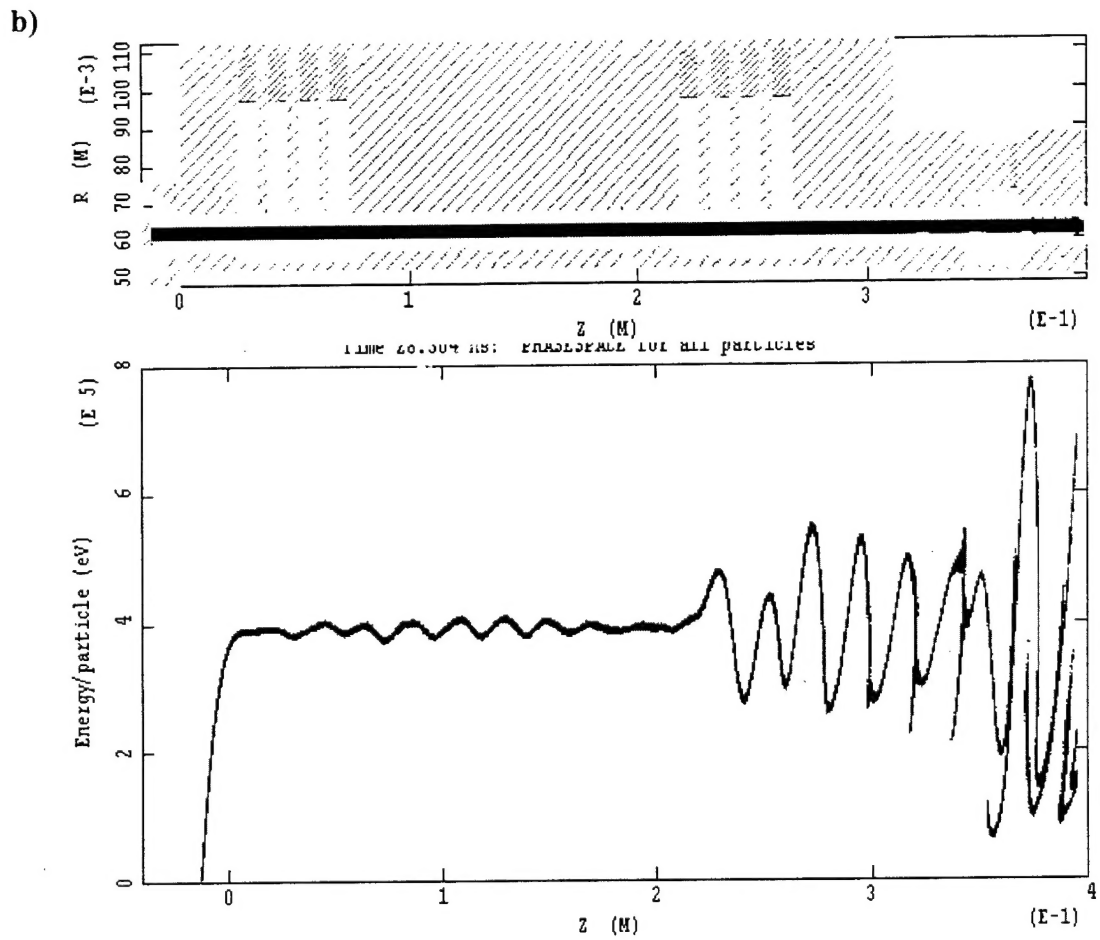
Simulation of a Sheet Beam Klystron.

Simulations of the TKA have been performed by Smithe & Pasour at MRC (see earlier reference). One tangential, but very beneficial aspect of the TKA, not possessed by any other high perveance klystron schemes, is cylindrical symmetry – at least for the operating mode. Thus 2-D simulation of this device is possible. One issue which resolved itself quickly with the TKA was the necessity of using multiple-cavity arrangements for both the buncher and output cavities. This may ultimately be necessary in the SBK, as well. Multiple cavity arrangements have been used in the past for the klystron output cavity, but are rarely used for buncher cavities. The figures below show: a) the tapered 4-cavity output coupler for the TKA, designed to operate in $2\pi/3$ phasing, b) a hot-test simulation with dual 4-cavity bunchers, followed by that same output coupler, with the input coupler omitted and replaced with low-level (4%) pre-modulation of the beam, and the energy of the beam has is travels down the TKA, and c) a similar run of just the penultimate buncher together with the output cavity, but using cylindrically symmetric PPM focusing, instead of solenoid magnet focusing. Note that the axis at $r=0$ is omitted from all these figures – one constantly must remind oneself that the lower conductor is actually the inner coax.

a)

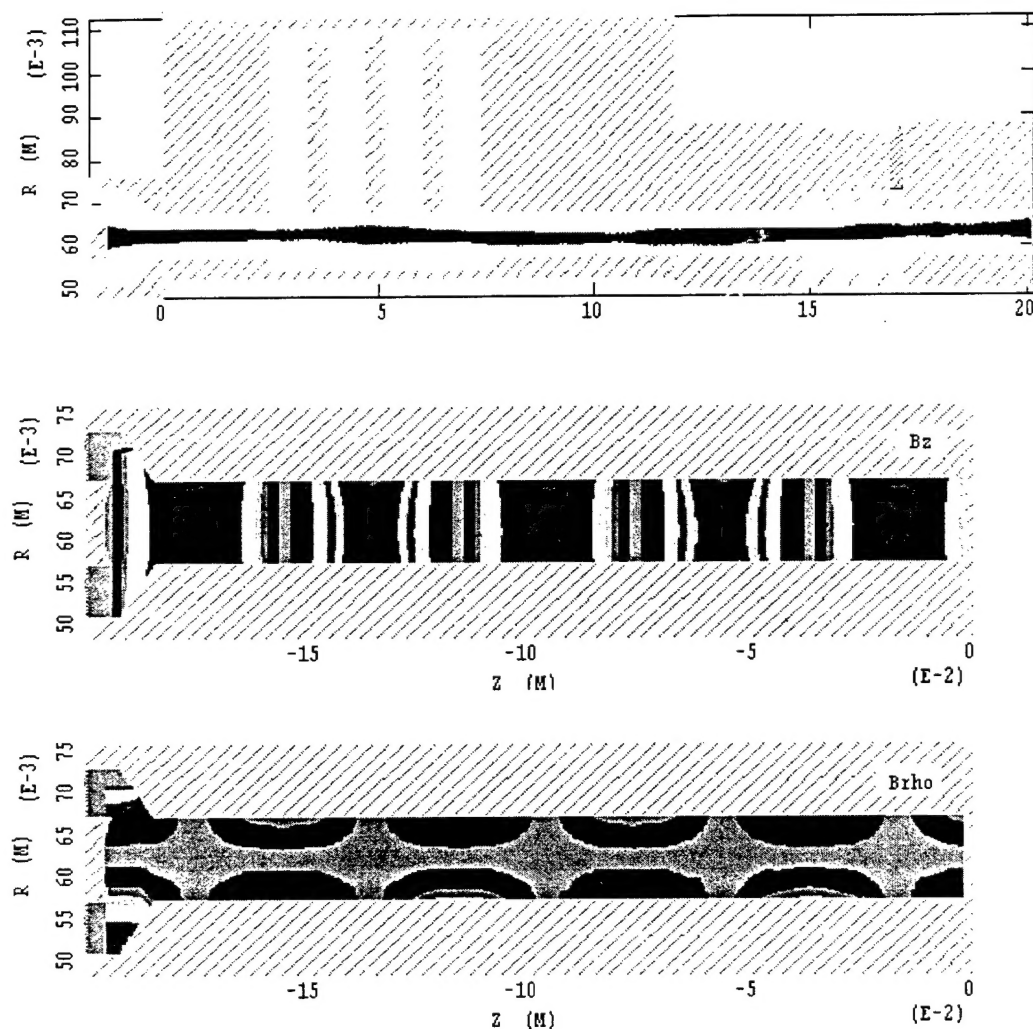


Carefully Tuned and Tapered Output Cavity for the Triaxial Klystron Oscillator. Note that the lower conductor is actually the inside coax.



Simulation of the TKA with two buncher cavities and the output cavity.

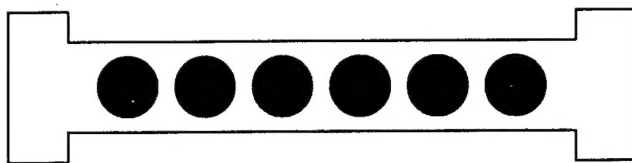
c)



Linear PPM focusing in the TKA. The method of using PPM focusing in a SBK is nearly identical.

The simulations of the GMBK and MBK are discussed at great length in the body of this final report, and will not be repeated here.

Finally, one might wish to consider the alternate GMBK geometry, in which multiple beamlets traverse an SBK-type cavity, rather than a coaxial cavity. In this case, the drift tubes are cutoff, which does alleviates one of the issues that did appear in both the SBK and TKA simulations, namely RF communication between cavities through the drift tube. Also, it would be possible to operate the SBK dumbbell-type cavity at a higher mode number, where the mode-spacing is greater, by placing the field nulls between the beamlets. One can even imagine operating in a mode where each beamlet is 180 degrees out of phase of its two neighbors, see the cartoon below. Such an operating mode could be nearly 40% higher ($\sqrt{2} - 1$) in frequency than if the cavity were run with all beamlets in phase. Obviously, this opposite-phase operating-mode is also possible with the original GMBK configuration, and could be used to increase its operating frequency. To the best of this author's knowledge, no investigations have been performed of GMBK configurations operating at higher modes, but this could be an area of future interest and research.



A speculative GMBK-like high permeance klystron configuration using an SBK-type cavity instead of a coaxial cavity. Using beamlets instead of a sheet beam can eliminate difficulties of RF transmission within the sheet beam drift tube. Alternating the phase of adjacent beamlets may permit operation at higher frequency than when all beamlets are in phase.

In conclusion, MRC has had a unique opportunity to be involved in the simulation of 4 difference high permeance klystron concepts within this past year, the GMBK, a 19-beam MBK, the SBK, and the TKA. On the surface, and perhaps fortunately, there has been little overlap in terms of operating parameters, nevertheless the ultimate push for a practical high permeance solution remains at the heart of each of these projects. While the MBK represents an incremental alteration to the conventional klystron, the SBK and TKA offer a significantly different approach, where it is easy to add permeance simply by lengthening the beam width, or perimeter, as may be the case. The GMBK is an interesting mix of the alternatives, maintaining the individual beamlets of the MBK, but arranging them in the same easy-to-scale geometry as the SBK or TKA.

References

-
- i "A 2-Gigawatt, 1-Microsecond, Microwave Source," by G. Caryotakis, E. Jongewaard, R. Phillips, G. Scheitrum, S. Tantawi N. C. Luhmann, Jr., in Multiple Beam Klystrons: The U. S. Version, Revised SLAC Report (November 1, 1996).
 - ii "The New generation of High Power Multiple Beam Klystrons," by Edward A. Gelvich, Ludvik M Borisov, Yevgeny V. Zhary, Anotoli D. Zakurdayev, Alexandr S. Pobedonostev, and Victor I. Poognin, IEEE Transactions on Microwave Theory and Technique, Vol. 41, January 1993, pg. 27.
 - iii "Gigawatt Multibeam Klystron (GMBK)," by G. Caryotakis, E. Jongewaard, R. Phillips, G. Scheitrum, S. Tantawi, and N. C. Luhmann, Jr., poster paper presented at 11th International Conference on High Power Particle Beams, Prague, Czech Republic, June 1996.